01

Deep penetration of metals by concentrated energy fluxes (a review)

© R.D. Seidgazov,[1] F.Kh. Mirzade,[1] G.G. Gladush[1,2]

[1]National Research Center „Kurchatov Institute“,
Moscow, Russia
[2]Joint-Stock Company „State Scientific Center of the Russian Federation Troitsk Institute of Innovation and Fusion Research“of the State Corporation Rosatom,
Troitsk, Moscow, Russia
e-mail: seidgazov@mail.ru fmirzade@rambler.ru

Received July 1, 2025
Revised September 29, 2025
Accepted November 1, 2025

This article discusses the current state of fundamental research into the phenomenon of deep melting caused by high-power energy sources, such as laser radiation and high-energy particle beams. This phenomenon is observed when the power density of these sources exceeds a certain threshold level, and the shape of the melted zone changes from shallow and semicircular to deeper and elongated, due to the formation of a hollow channel through which the beam penetrates deep into the metal. The focus is on the results of studies of the hydrodynamic aspects of melting channel formation and its dynamic behavior in technological processes. Various capillary effects, including thermocapillary and electrocapillary, can determine the hydrodynamics of technological processes under various conditions and at different stages. The results of these fundamental studies are consistent with experimental data across a range of technological powers, demonstrating the inconsistency of the widely held assumption in the engineering community that melting channel formation is due to intense evaporation and removal of melt by the high recoil pressure of a vapor flow.

Keywords: laser radiation, thermocapillarity, metal, melt, technology, deep penetration, keyhole, pores.

DOI: 10.61011/TP.2026.03.63150.165-25

Introduction

The phenomenon of deep penetration (DP) forms the basis of the keyhole mode of metal processing in laser and electron beam technologies, which are in demand in the aerospace, nuclear, energy, and defense industries; shipbuilding; engine building; medicine; etc. The prospects for their application and further improvement are associated with digitalization and the development and implementation of scientifically grounded guidelines for the selection of optimal process parameters [1,2]. The DP phenomenon is essentially a threshold change in shape of the molten region: instead of being shallow and semicircular (in the subthreshold conduction mode), it becomes narrow and elongated (Fig. 1) due to the formation of a hollow channel (keyhole) through which the beam energy penetrates deep into metal. In this case, the depth-to-width ratio of the molten zone (L/D) exceeds unity and may reach a level of several dozen.

The DP mode is implemented in welding technologies (laser, electron beam, hybrid laser-arc) and in additive processes of selective melting of metal powders with a laser or an electron beam. Laser cutting of thick metals may also be regarded as a technology of this kind, since it is characterized by a strong perturbation of the melt hydrodynamics when melt products are removed with a gas jet [3].

The advantages of the DP mode include increased productivity and process efficiency, the capacity to weld together thick parts in a single beam pass, smallness of the heat-affected zone, minimal thermal deformation, and improved degassing of the melting zone. In additive manufacturing with selective melting of powder layers, this mode allows one to enhance productivity by increasing the thickness of the powder layer and raise the strength and wear resistance of the finished product by improving the bond between layers, refining grains, and altering the microstructure. The disadvantages of this mode are the instability of a keyhole and the formation of pores, which

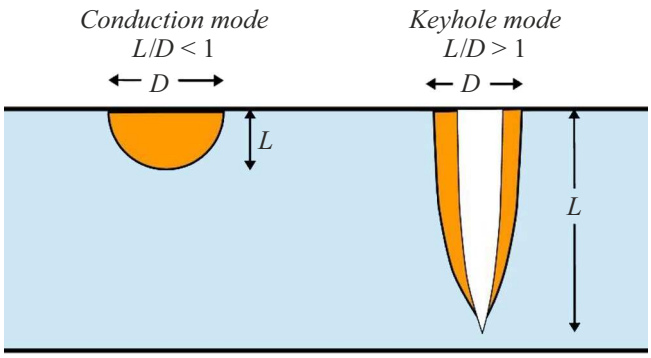

Figure 1. Schematic diagram of melting zones corresponding to different melting modes.

make it difficult to manufacture products of the highest quality and require greater efforts from process engineers to minimize and eliminate pores.

The boundaries of the range of process parameters within which the DP mode may be implemented are set by radiation power P, focal spot size d, and the metal properties. The lower boundary of this range is associated with the transition between melting modes and is traditionally characterized by threshold power density $q_{th}(d)$ that implies a quadratic dependence $P_{th}(d) \sim d^2$, where P_{th} is the threshold power. Since this dependence does not reflect the reality, the $q_{th}(d)$ values are accurate only within a very narrow range of d variation. It was demonstrated in [4] that linear dependence $P_{th}(d) \sim d$ characterizes the threshold transition more accurately. However, the maximum accuracy within a two-order-of-magnitude range of d variation is achieved with $P_{th}(d) \sim d^{4/3}$ (see Section 8). The upper limit of the technological range, which is associated with the onset of unwanted melt splashing and droplet dispersion, remains unexplored. Under typical laser welding conditions ($d \sim 500\,\mu$m) for steel samples, this boundary corresponds to $q_{spl} \sim 3\,\text{MW/cm}^2$ [5] (or $P_{spl} \sim 6000\,\text{W}$). In the present review, we examine the hydrodynamic processes within the $q_{th}(d) < q < q_{spl}(d)$ ($P_{th}(d) < P < P_{spl}(d)$) technological range.

The research into technological processes in the DP mode is focused on accelerated assimilation of new technologies and relies primarily on engineering methods. Since insufficient attention is paid to fundamental research, the current advances are intertwined with contradictory conclusions made by specialists coming from various fields of knowledge, sciences, and schools. To resolve the observed contradictions, one needs to analyze and systematize a large body of available research results and identify general trends. In this review, we discuss the results of fundamental studies into the DP phenomenon that reveal the mechanism of material self-organization under the influence of highly concentrated energy fluxes, where each technology is considered as a particular manifestation of the general mechanism.

The formation of a keyhole is a multiphysical nonequilibrium process with moving phase boundaries, which includes heat and mass transfer, surface phenomena, complex hydrodynamics, the dynamics of evaporation and vapor outflow, thermal emission of charges, the formation of plasma and the interaction of radiation with it, electrodynamic processes, waveguide propagation of laser radiation in the keyhole, etc. Physical modeling of such a complex phenomenon is a difficult problem, which is unlikely to be solved without the use of numerical methods and without reliable data of the mechanism of the phenomenon. At present, computer modeling of the DP mode is used successfully to solve technological problems based on the determination of temperature fields for prediction of thermal stresses, deformations, and crack formation. The reproduction of hydrodynamic fields is needed to predict the formation of hidden defects of hydrodynamic origin (pores and cavities) and prevent their emergence in the process of manufacture of high-duty products. However, owing to the methodological confusion that complicates the study of DP, this problem has not been solved yet.

1. Methodological aspects of development of DP concepts

The knowledge of temperature fields and cycles is considered in DP technologies to be the basis for understanding all associated metallurgical processes related to the physics of metals, chemical kinetics, plasma physics, etc. This list normally does not include hydrodynamic fields, since their influence is assumed to be insignificant. The concept had been formed by the time when the DP phenomenon was starting to be incorporated into production processes in the 1970s. N.N. Rykalin has proposed to treat the temperature distribution in DP as a result of influence of two heat sources: a point source on the surface and a source distributed linearly over depth. This makes it possible to obtain approximate temperature fields analytically even when data on the physics of keyhole formation are lacking. A realistic numerical simulation of the keyhole is needed to increase the accuracy of calculations. An approximation based on the calculation formalism of the ablation mechanism, where a keyhole is assumed to form as a result of displacement of the melt by the recoil vapor pressure, was used for this purpose [6–8]. At the same time, attention was drawn in [9] to the possibility that a keyhole is maintained by thermocapillary (TC) forces moving the melt. This was a response to the reported measurements of vapor pressure in the keyhole [10], which turned out to be orders of magnitude lower than the values required to form the keyhole by ablation pressure. These measurements questioned the relevance of the ablation mechanism to DP and have been verified later by similar measurements performed in [11,12]. It is worth noting here that all experimental confirmations of the ablation mechanism were obtained outside the technological power range (at very high power densities exceeding $10^8\,\text{W/cm}^2$ [13]). Thus, the insignificance of ablation pressure under process conditions has been demonstrated experimentally as early as in the 1970s, paving the way for understanding the TC mechanism of keyhole formation. This issue was debated at the turn of the 1970s and 1980s, and different views on the DP phenomenon and approaches to its examination were proposed. However, while some were interested in finding a suitable physical mechanism, others needed a computational method to simulate a keyhole for numerical determination of temperature fields. These two different approaches proved difficult to reconcile, and the debate became heated. The already available experimental data contradicted the ablation mechanism and testified in favor of the TC mechanism. However, a physically sound mechanism was not required to simulate a keyhole in the process of numerical reproduction of temperature fields for solving thermal problems of mass

engineering. A calculation formalism based on any of the mechanisms is sufficient for this purpose. Since the ablation mechanism is the simplest, the TC mechanism was rejected.

A wide range of professionals perceived this verdict as a scientific conclusion regarding the physical mechanism of DP. Process engineers, who regularly observed the emergence of a bright plasma torch of metal vapor in the DP mode, even regarded it as a statement of the obvious. As a result, contradictions found between the ablation mechanism and the experimental data were ignored as erroneous. Thus, the concept of ablation mechanism being the dominant one in the DP phenomenon has become entrenched in scientific and technical literature and engineering textbooks. Opting for the ablation mechanism as a calculation formalism for keyhole simulation, the researchers limited themselves to the reproduction of temperature fields only. However, these limitations were not understood, and the ablation mechanism was also used in numerical modeling of hydrodynamic fields (i.e., outside the range of applicability).

The demand for numerical simulation of hydrodynamic processes arose in a relatively confined but very important sector of technological engineering associated with the manufacture of high-duty products that meet the highest quality requirements and are a marker of technological leadership of industrialized countries. It is assumed that this should help eliminate the main drawback of the DP mode: unwanted generation of pores by an unstable keyhole. Acting as stress concentrators, pores reduce the reliability and service life of critical parts and components operating in high-stress environments. The production parameters need to be optimized in order to suppress the formation of pores. At present, this is achieved through trial and error, which is typical for the initial stage of technology development (when a proper theory has not been formulated yet), but requires the examination of a large number of samples over a long period of time and a significant investment of effort, time, and resources. This poses a challenge to additive manufacturing, undermining their capabilities and prospects for digital transformation of industry. The response must be an accurate prediction of pore formation based on reliable knowledge of the nature of the technological process. However, researchers solving this problem encountered difficulties in numerical reproduction of hydrodynamic fields, citing the lack of precise knowledge of the driving forces affecting the flow of fluid, which limits the reproduction of hydrodynamic processes to just a few qualitative effects, as the reason for their failures [14]. These failures may arise from an overestimation of significance of the ablation mechanism. This is evidenced not only by the above-mentioned data on the insignificance of vapor pressure in the keyhole [10–12] and other reports revealing little evaporation in the keyhole [15,16], but also by the lack of reliable validation of calculation models of the DP mode [17,18].

At the same time, fundamental research into the TC mechanism was ongoing, and the obtained results and conclusions were in close agreement with experimental data. We outline them briefly in the present review, starting with model experiments [19,20], which demonstrated the fundamental possibility of forming a keyhole with insignificant evaporation. These data were used to construct a theoretical evaluation model for the formation of a keyhole via melt removal by TC forces [21,22], and estimates verifying the relevance of the TC mechanism under process conditions were obtained. Studies into the initial stage of metal melting in the DP mode confirmed the formation of a shear structure of TC flow in the irradiation zone and revealed the reason for nonlinear dynamics of keyhole growth under point impact [23]. A relation for the conditions of threshold transition to the DP mode was obtained [24], and its correspondence to experimental data was confirmed. It was established that the generation of pores by an unstable keyhole is the result of excitation of capillary-wave oscillations of the melt [25]. The key patterns of pore generation were revealed [26,27], and the obtained relations were verified by comparison with experiments. A criterion for termination of pore formation, which sets the position of a window in the coordinates of process parameters and opens up an opportunity to digitalize routine procedures of development of technologies for manufacture of high-duty products, was defined.

The TC flow structure at DP has a feature that distinguishes it from the TC flow structure in the subthreshold conduction mode [19–22]. If this feature is neglected, the commitment to take into account the actions of both mechanisms (ablation and TC) may also lead to erroneous results and conclusions regarding their contributions [28–31], which makes the real hydrodynamic picture even harder to see. In the mean time, correct supercomputer calculations [32] carried out at the Livermore Laboratory with the aim of testing the idea of cavity formation by the TC mechanism [20] confirmed that a deep cavity may be formed in metal under the influence of just the TC mechanism with the contribution of the ablation mechanism being immaterial. The reason for underestimation of the significance of the TC mechanism in [28–31] was analyzed in [33], and it was concluded that this error is attributable to the use of a coarse computational grid inconsistent with physically justified requirements as to the discretization of the computational domain.

Fundamental studies into the role of capillary phenomena in DP processes provided an opportunity to interpret a number of effects and correlations that could not be explained using the ablation and TC mechanisms. Among them are the synergistic effect in hybrid laser-arc processing [34] and the empirically observed correlations of the penetration depth with the ambient pressure variation, the characteristics of near-surface plasma, the emission current signal [35], and the direction and strength of the external electric field [36]. To gain an insight into these effects and correlations, one just needs to consider that surface tension depends not only on surface temperature, but also on electric potential. This idea is illustrated in [37] by the hypothesis of acceleration of TC flow by electrocapillary

forces, which are induced by dependence $\sigma(\varphi)$ of surface tension on electric potential that is distributed non-uniformly along the surface. This hypothesis points to a potential way to develop and improve methods for monitoring and managing technological processes.

2. Evolution of a keyhole under the point impact of continuous-wave laser radiation

Visual observation of DP of metals is hampered by difficulties associated with high temperatures in the irradiation zone. Model experiments provide an opportunity to avoid these complications. Specifically, a model experiment on laser melting of paraffin, where imaging is facilitated by the lack of laser plasma and the optical transparency of molten paraffin, proved informative. The results of observation of the evolution of a keyhole in paraffin with a depth up to 3–5 mm formed by stationary and continuous-wave laser radiation with a power of 20–30 W were presented in [19,20]. The peculiar pattern of evolution of the keyhole in paraffin, which ends with flow-in and collapse despite the fact that irradiation is still ongoing, has been noted for the first time in monograph [38]. A toroidal vortex flow with TC recirculation of the melt is formed instead of the vanished keyhole (Fig. 2). A low rate of paraffin vapor outflow (~ 1 cm/s) was recorded during the formation of the keyhole, which confirmed the infeasibility of forming a keyhole by recoil vapor pressure. The intermediate stage with excitation of melt oscillations in the keyhole and alternating capture of gas bubbles, which

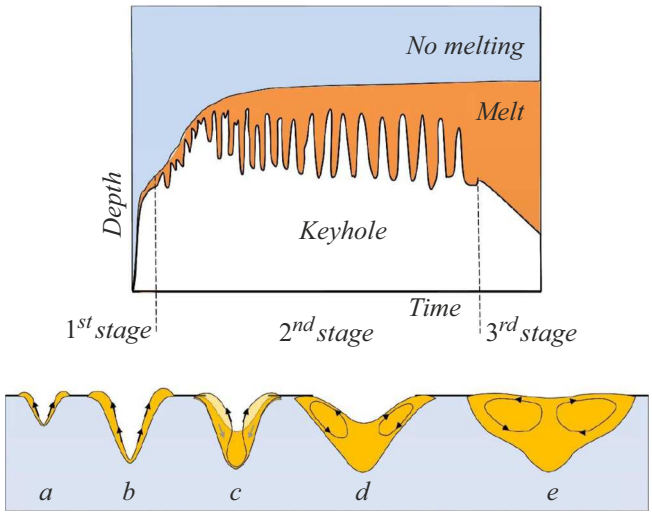

Figure 2. Evolution of the molten pool. Variation of depth of the keyhole in paraffin and appearance of the molten pool with time under the influence of continuous-wave laser radiation with a power of 30 W. a, b — 1st stage, crater formation; c — 2nd stage, excitation of melt oscillations in the keyhole; d, e — 3rd stage, keyhole collapse as a result of flow-in with irradiation still ongoing.

has a clear similarity with the generation of pores by an unstable keyhole in actual processing of metals, is of interest. Thus, a simple model experiment provides an insight into the physics of complex hydrodynamic processes in real technologies.

The change in nature of hydrodynamic processes allows one to distinguish three stages of evolution of the keyhole. The first stage is characterized by keyhole growth. With insignificant evaporation, just a slight influence of recoil vapor pressure, and an insignificant contribution of the ablation mechanism, TC removal of the melt from the irradiation zone is the only feasible driving force behind the keyhole formation. This is confirmed by the flow-in and vanishing of the keyhole at the final stage of evolution, which is observed with laser irradiation still ongoing. An evaluation theoretical model was constructed, which provided an opportunity to make confirmatory estimates for both paraffin penetration and penetration of various metals [19–22]. The fundamentals of this model are presented in Section 3. The intermediate (second) stage of evolution of the keyhole is characterized by the excitation of intense oscillations in the melt layer on its walls, which may lead to bubble capture (see Section 6). Data on the hydrodynamic processes at this stage are of particular importance for solving the problem of pore formation in the DP mode in development of process technologies for manufacture of high-duty products (see Sections 6, 10).

3. TC mechanism of deep laser penetration

The TC effect is well known as a mechanism of melt recirculation (Marangoni convection) in the subthreshold conduction mode. This flow forms if a metal is heated non-uniformly and surface tension $\sigma(T)$ is temperature-dependent. Its structure include a near-surface TC flow and a reverse flow with friction against the bottom. The action of TC forces on the surface determines the flow direction and depends on the sign of temperature coefficient of surface tension $\sigma_T = \partial\sigma/\partial T$. It is always negative for pure metals ($\sigma_T < 0$) and specifies the direction of TC forces from hot metal at the center of the irradiation spot to the colder part at the periphery of the irradiation spot. The sign of σ_T may change to positive ($\sigma_T > 0$) under the influence of surfactants, impurities, or contamination. The TC flow is then directed from the periphery of the irradiation spot to the center. A positive σ_T is characteristic of alloys heated from melting point T_M to a certain point of inversion of the sign of σ_T, above which the sign of σ_T always changes to negative, since the surface tension understandably tends to zero at the critical temperature. The σ_T sign inversion point is normally located $\sim 100–300°$ higher than T_M; therefore, it remains lower than boiling point T_B, which is characteristic of heating of the keyhole walls in the DP mode (according to the experimental data from [39]). This is the reason why the sign of σ_T is always negative ($\sigma_T < 0$)

in the DP mode, and the TC flow is directed from the center of the molten pool with characteristic temperature T_B to the periphery with temperature T_M. Thus, condition $\sigma_T > 0$ may be satisfied only in the conduction mode of melting of metals.

Let us consider the simultaneous motion of two phase boundaries: the melting front, which moves with velocity V_M, and the free surface deforming at rate V_S by virtue of conservation of mass due to the TC melt spreading. Note that the formation of a vortex flow with closure of flow lines is non-instantaneous and requires a certain time. At the initial stage of melting, the TC flow always has a shear structure, which leads to melt removal from the center of the irradiation zone to the periphery and deformation of the surface. Owing to the conservation of mass, deformation rate V_S is small compared to velocity V_M of the melting front at a low TC flow velocity V; i.e., $V_S < V_M$. Under this condition, the thickness of the melt layer increases with time, which implies further closure of flow lines and formation of TC melt recirculation. The pattern changes if TC flow velocity V is so high that the level of $V_S = V_M$ is reached. In this case, both phase boundaries move while maintaining the thickness of the molten layer and the shear structure of TC flow (without the closure of flow lines and the emergence of a reverse bottom flow). This flow structure is characteristic of the removal of melt from the irradiation zone and the formation of a cavity [19–22] (Fig. 3). As a cavity grows in metal, laser radiation gets reflected multiple times from the walls and the effective absorption increases to $A = 0.6–0.9$ [40,41], which helps maintain a high deformation rate under condition $V_S = V_M$. The characteristic TC flow velocity is determined from the balance of surface TC forces and resistance forces of the viscous sublayer:

$$V \cong \frac{\sigma_T}{\eta}\frac{\partial T}{\partial r}\delta,$$

where η is the dynamic viscosity, $\sigma_T = |\partial\sigma/\partial T|$, $\partial T/\partial r$ is the temperature gradient along the melt surface, and δ is the viscous sublayer thickness that is equal to molten layer thickness h in the case of a shear flow structure; i.e., $\delta = h$. If the molten layer thickness is small ($\delta = h \ll d$), the temperature gradient may be estimated as $\partial T/\partial r \approx Aqh/(\lambda d)$, where Aq is the absorbed power density ($A = 0.6–0.9$ [40,41] is the effective absorption in the keyhole), λ is thermal conductivity, and d is the focal spot diameter. The velocity of shear TC flow may then be written as

$$V \cong \frac{\sigma_T A q \delta^2}{\lambda \eta d}. \qquad (1)$$

Thickness $h = \delta$ is determined from equality $V_S = V_M$ upon the formation of a cavity

$$\delta = h = \sqrt[4]{\frac{\lambda \chi^{1/2}\eta^{3/2}d^2}{(Aq\rho^{1/2}\sigma_T)}}, \qquad (2)$$

where χ is thermal diffusivity and ρ is density. Relations (1) and (2) allow one to estimate the velocity of shear TC flow,

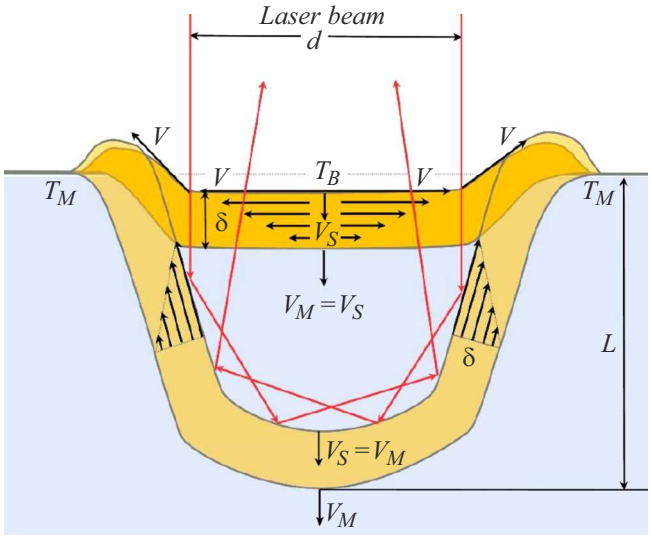

Figure 3. Thermocapillary shear flow of melt and cavity growth in steady-state conditions at $h(t) = \delta(t)$ and $V_S(t) = V_M(t)$ with multiple reflections of laser radiation from the walls.

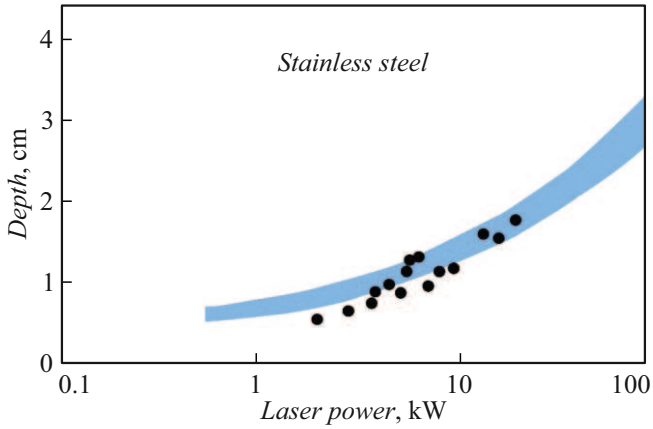

Figure 4. Maximum depth of laser penetration of steel calculated according to the TC penetration model [22] with account for the spread of data on material properties. Points correspond to the experimental data from [43].

its thickness $h = \delta$, cavity growth rate V_S, and threshold power $P_{th}(d) = q_{th}(d)(\pi d^2/4)$ of transition to the DP mode (see Section 8). The obtained estimates correspond to experimental values within the technological power range [19–22]. The TC model provides an opportunity to estimate the maximum keyhole depth. The nature of dependence of the maximum depth of steel penetration on laser beam power was established in the form of $L \sim P^{0.7}$ in [42] (Fig. 4) through analysis of a set of empirical data. A close analytical dependence $L \sim P^{2/3}$ was obtained in [22] with the assumed TC mechanism of DP. This dependence is represented in Fig. 4 by the shaded region, which accounts for the spread of data on the properties of steel. The

correlation of calculated and experimental data verifies the TC mechanism of DP.

4. Evolution of hydrodynamic parameters at the initial stage of keyhole formation

The evolution of penetration parameters and their influence on the growth of a cavity at the initial stage of melting were analyzed in [23]. The process of metal melting by stationary and continuous-wave radiation focused into a spot with a diameter d was considered; curves characterizing the evolution of the following parameters at constant metal properties are plotted alongside each other in Fig. 5: surface temperature $T(t)$, TC flow velocity $V(t)$, melting front velocity $V_M(t)$, surface deformation rate $V_S(t)$, thicknesses of molten layer $h(t)$ and viscous sublayer $\delta(t)$, and DP (keyhole) depth $L(t)$.

Melt surface temperature. Radiation is absorbed within a very thin layer on the metal surface. The propagation of a heat wave over distance x in time t is approximated as

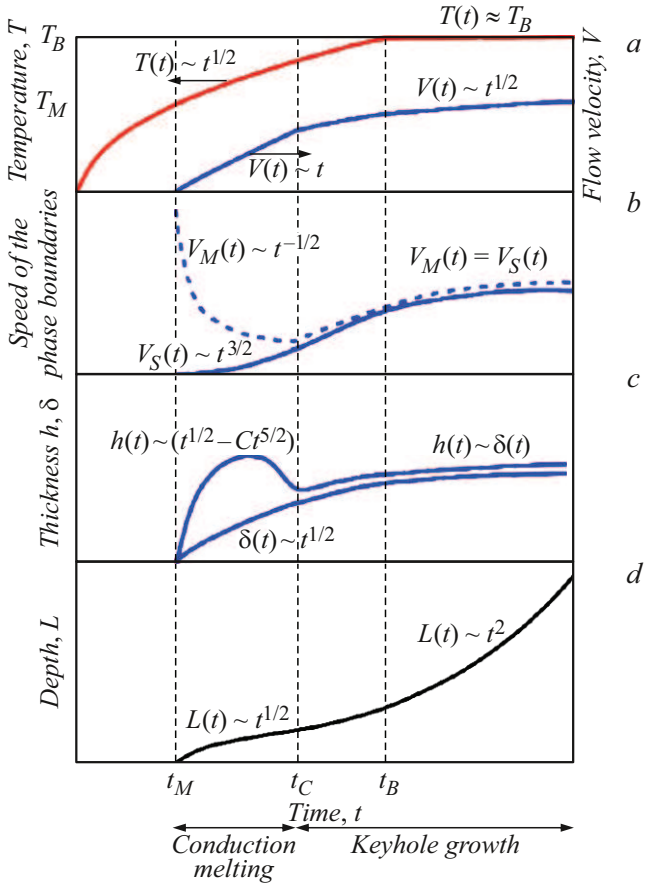

Figure 5. Evolution of melting parameters in the DP mode [23]: *a* — surface temperature $T(t)$, TC flow velocity $V(t)$; *b* — melting front velocity $V_M(t)$, surface deformation rate $V_S(t)$; *c* — thicknesses of molten layer $h(t)$ and viscous sublayer $\delta(t)$; *d* — keyhole depth $L(t)$.

$x(t) \approx (\chi t)^{1/2}$. The change in surface temperature induced by a heat source with constant power density q is

$$\Delta T(t) \cong \frac{2Aq}{\lambda}\sqrt{\frac{\chi t}{\pi}}.$$

If A, λ, and χ are assumed to be constant, the temperature variation is $\Delta T(t) \sim t^{1/2}$. The process of melting commences at temperature T_M and time point t_M. At time t_B, surface heating reaches saturation at boiling point T_B [39]. Therefore, two intervals may be distinguished in the melting process: $t_M < t < t_B$ with temperature variation $T(t) \sim t^{1/2}$ and $t > t_B$ with temperature saturation at boiling point $T(t) = T_B$ (Fig. 5, *a*).

Thickness of the viscous sublayer. When TC flow commences, the surface force is transferred by viscous forces to the lower layers. If convective heat transfer is neglected, the nature of their propagation through thickness δ of the viscous sublayer is similar to that of the propagation of temperature; i.e., at $V > 0$, $\delta(t) \approx (\nu t)^{1/2}$ or $\delta(t) \sim t^{1/2}$ (Fig. 5, *c*).

Thermocapillary flow velocity. The velocity of thermocapillary flow starts to increase in accordance with relation (1) at time point t_M. Notably, it grows linearly with time in the $t_M < t < t_B$ interval, since $V(t) \sim T(t) \sim \delta(t) \sim t$. At $t = t_B$, the temperature reaches saturation $T(t) = T_B$; at later points in time ($t > t_B$), it remains unchanged, while the TC flow velocity increases with a nonlinear deceleration over time $V(t) \sim \delta(t) \sim t^{1/2}$ (Fig. 5, *a*).

Surface deformation rate. Radial spreading of the TC flow with velocity V at a viscous sublayer thickness of δ causes deformation of the liquid surface, which proceeds at rate $V_S(t)$, and the formation of a cavity (see Fig. 3). The mass conservation condition is written as $V_S(t)(\pi d^2/4) = V(t)\delta(t)\pi d$, which yields $V_S(t) = 4V(t)\delta(t)/d$. At $V(t) \sim t$ and $\delta(t) \sim t^{1/2}$, the surface deformation increases with nonlinear acceleration $V_S(t) \sim t^{3/2}$ in the $t_M < t < t_B$ interval, and surface heating at $t > t_B$ reaches saturation at boiling point T_B. Therefore, the $V_S(t)$ velocity increase slows down (by virtue of $V(t) \sim t^{1/2}$ and $\delta(t) \sim t^{1/2}$) and becomes linear: $V_S(t) \sim t$ (Fig. 5, *b*).

Molten layer thickness. Molten layer thickness $h(t)$ is set by the motion of two phase boundaries. In a moving frame of reference associated with the absorbing surface, thickness $h(t)$ increases as the melting front moves deeper into the metal with velocity $V_M(t) \approx (\chi/t)^{1/2}$ and decreases due to deformation of the surface at rate $V_M(t)$. Using $V_M(t)$, $V_S(t)$, and $T(t)$ and denoting $C = 8Aq\nu/\pi^{1/2}\lambda d$, we obtain

$$h(t) = (V_M(t) - V_S(t))t \approx (\chi t)^{1/2} - \frac{8Aq\chi^{1/2}\nu}{\pi^{1/2}\lambda d}t^{5/2}$$

$$= \chi^{1/2}(t^{1/2} - Ct^{5/2}).$$

Thus, the onset of melting is marked by an increase in $h(t)$ due to rapid (but slowing down nonlinearly) propagation of a heat wave $h(t) \sim t^{1/2}$. However, thickness $h(t)$

then decreases abruptly due to nonlinear acceleration of deformation rate $V_S(t) \sim t^{3/2}$. As a result, the growing viscous sublayer adheres to the melting boundary at time point t_C. The fulfillment of no-slip condition $h(t) = \delta(t)$ completes the formation of shear TC flow (Figs. 3, 5, *c*). Starting from t_C, two phase boundaries separated by the viscous sublayer are engaged in dynamic interaction. The viscous sublayer limits the rate of surface deformation by viscous deceleration of TC flow, but also maintains a proper level of the melting front velocity by keeping thickness $h(t)$ at the lowest possible level and thereby ensuring the maximum possible heat flux to the melting front. Thus, no-slip condition $h(t) = \delta(t)$ for the viscous sublayer leads to effective removal of the melt from the irradiation zone and to the onset of growth of a cavity with equal velocities $V_M(t) = V_S(t)$. No-slip condition $h(t) = \delta(t)$ is violated when the maximum keyhole depth is reached and the process of removal of the melt from the keyhole throat ceases.

Penetration depth. Point of adhesion t_C divides the melting process into two phases: preparation of shear TC flow ($t_M < t < t_C$) and the phase of steady keyhole growth ($t > t_C$) (Fig. 5, *d*). The first one is characterized by an insignificant surface deformation with an increase in penetration depth due to thermal conductivity: $L(t) \approx h(t) \sim t^{1/2}$. The second phase is associated with the keyhole growth and nonlinear acceleration of the penetration depth: $L(t) \approx V_S(t)t \sim T(t)\delta^2(t)t \sim t^{5/2}$ at $t_M < t < t_C$ and $L(t) \sim \delta^2(t)t \sim t^2$ at $t > t_B$. Apparently, a jump in effective absorption A resulting from radiation capture by a cavity accelerates the keyhole growth additionally (Fig. 5, *d*). The existence of two phases of penetration with a characteristic break in the $L(t)$ evolution curve is observed in experiments with metals [43] (their results are analyzed below in Section 6).

Thus, the above analysis confirms that it is the TC nature of flow that ensures a high rate of surface deformation in the DP mode, contributes to maintaining the shear structure of TC flow, and governs the formation of a keyhole. Notably, this keyhole exists only in a short time interval within which the shear structure of TC flow is preserved after adhesion of the viscous sublayer to the melting front.

5. Experimental determination of the mechanism of deep penetration in metals

Ablation and TC mechanisms differ in the application of forces to the free surface of the melt. The force of ablation recoil vapor pressure acts along the normal to the free surface, while TC forces are directed tangentially. This shapes the specifics of evolution of a cavity under point and long-term exposure to radiation, which allow one to establish experimentally the dominant mechanism of keyhole formation. If the ablation mechanism is dominant, the keyhole evolution will involve two stages: initial growth proceeding until the maximum depth is reached and subsequent quasi-steady existence of a cavity under long-term exposure to radiation (Fig. 6). This quasi-steadiness of a cavity under the influence of recoil vapor pressure was observed in model experiments on the effect of continuous-wave laser radiation on liquids [44]. The lack of a melting boundary makes experiments with liquids an inadequate model of the DP phenomenon. The formation of a melting boundary upon substitution of a liquid with paraffin in experiments [19,20] alters radically the keyhole evolution. It turns out that the keyhole is short-lived and vanishes as a result of flow-in despite the fact that irradiation is still ongoing. Following the keyhole collapse, TC flow takes the form of vortex recirculation with a reverse bottom flow characteristic of the conduction mode. This type of evolution reflects the dominance of the TC mechanism with an insignificant contribution of the ablation mechanism.

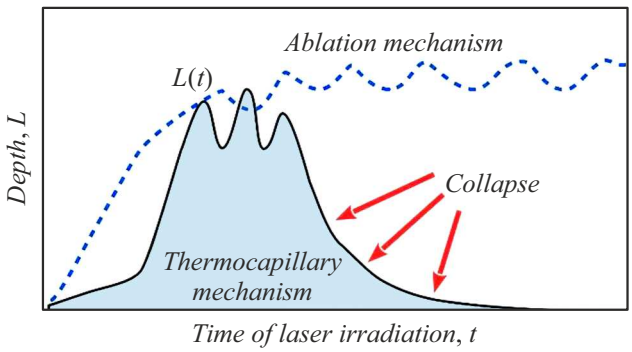

Figure 6. Evolution of the keyhole with the ablation (dashed curve) or TC (solid curve) mechanisms being dominant.

To extend the conclusions drawn from model experiments to metal processing, one needs to confirm experimentally that the nature of keyhole evolution in metals is similar. An experiment with a sample in the form of a sandwich of two tightly pressed plates of titanium and transparent sitall was performed for this purpose. Laser radiation with a power of 1.5 kW was focused on titanium near its contact with sitall [45]. The results of video recording of the keyhole evolution in titanium are presented in Fig. 7. Thermal traces of a keyhole at the stage of its growth, which are created by the glow of metal heated to a high temperature, were imaged. The maximum depth of the thermal trace is 4.5 mm and is much greater than its width, indicating the formation of a keyhole. When the keyhole reaches its maximum depth, the image of its thermal trace is erased throughout the entire height by a fast darkening wave moving from right to left (similar to a shutter). This type of image fading cannot be represented by a time dependence of depth; therefore, it is denoted by a shaded region. The sudden vanishing of the image may be attributed to spiral flow-in, which will be discussed in Section 6. The penetration process was recorded over a sufficiently long time interval (~ 2 s) to ensure that the keyhole could not be re-formed.

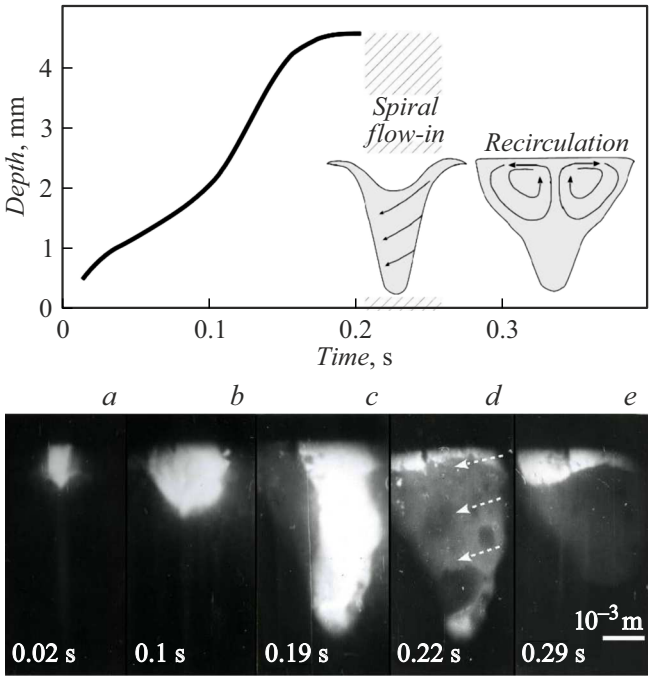

Figure 7. Evolution of a keyhole in titanium produced by 1.5 kW laser radiation with final collapse and transition to melt recirculation [45]. The direction of melt flow is indicated by arrows.

6. Main stages of keyhole evolution

Let us discuss the specific hydrodynamic processes at each stage of keyhole evolution with a focus on the conditions of transition from one stage to another.

The 1st stage is characterized by the growth of a cavity with rapid deformation of the surface due to melt removal by shear TC flow and was characterized theoretically in [19–22]. The evolution of melting parameters and the formation of shear TC flow at this stage [23] (Fig. 5) were analyzed in Section 4, where this stage was divided into two phases: the initial phase of shear flow preparation with motion of the melting front driven by thermal conductivity and the phase of steady keyhole growth with a high melting front velocity $V_M = V_S$ due to rapid deformation of the free surface and cavity growth. The 1st stage ends with the cessation of TC melt removal from the keyhole throat due to the suppression of temperature gradient on the keyhole walls with increasing depth.

The 2nd stage is associated with transitional processes of transformation of shear flow to melt circulation and flow-in at the final 3rd stage of evolution. The 2nd stage is characterized by the excitation of capillary-wave oscillations of the melt layer on the walls of a deep cavity [19,20,25–27]. It starts with the cessation of melt removal through the keyhole throat and accumulation of liquid mass in the upper part of the keyhole. This causes a local separation of the viscous sublayer from the melting boundary (i.e., local disruption of the shear structure of flow). A reverse wall flow, which emerges at the site where the viscous sublayer gets separated, transfers the excess mass to the bottom of the keyhole and allows the viscous sublayer to re-adhere at the keyhole throat. The displaced mass induces separation of the viscous sublayer at the bottom of the keyhole. For this reason and due to the „scissors effect," the maximum amplitude of oscillations of the molten layer, reaching 30 %–40 % of depth L, is found in the root part of the keyhole. Short-term alternating keyhole collapses with the capture of a gas bubble, which occur when the crests of waves from the opposite walls come into contact in the upper part of the keyhole (Fig. 8), are possible in this case.

Such capillary-wave oscillations in technological processes may induce keyhole instability with unwanted pore generation, which is recognized as the main drawback of the DP mode. This is what makes the research into the 2nd stage of keyhole evolution practically relevant. The buildup of capillary waves is the result of TC instability [46–48]. Owing to incompressibility of the melt, transverse liquid motion is induced by fluctuation TC motion of the melt along the free surface, which leads to the emergence of crests and troughs on the melt surface. Since the molten layer features a constant negative transverse temperature gradient, the surface temperature increases at crests and decreases at troughs, establishing the preconditions for TC buildup of capillary waves.

It was demonstrated in [32] that resonant amplification of capillary oscillations at the 2nd stage of evolution may be used to raise the efficiency of metal drilling by choosing the proper frequency of modulated laser radiation. The main patterns of pore generation in real technological DP processes were established in [26,27], and the condition for cessation of pore generation, which determines the position of the technological window in the coordinate system of key process parameters, was formulated. The results were indicative of the potential to predict the technology window position and provided a scientific basis for improving the processing techniques.

The 3rd stage is associated with the final collapse of the keyhole as a result of flow-in, which is accompanied by closure of flow lines and stable recirculation of the melt [19,20,45]. The process of keyhole collapse in paraffin is fairly prolonged, which makes it easier to examine this stage. The collapse in metals proceeds rapidly due to their low viscosity, complicating experimental studies. High-speed synchrotron (X-ray) imaging was used in [43] to observe the evolution of a keyhole in metal. The obtained evolution curve is shown in Fig. 9. The first two stages are clearly distinguished in it.

The 1st stage features a well-pronounced preliminary phase of slow melting and a subsequent keyhole steady growth phase. This is consistent with the analysis of formation of shear TC flow presented in Section 4 (Fig. 5, *d*). The 1st stage of keyhole formation then passes into the 2nd stage with excitation of oscillations of the melt in the keyhole. At this point, tracking of the keyhole evolution was stopped for an unknown reason. The authors made no mention of either a forced shutdown of the laser source or a

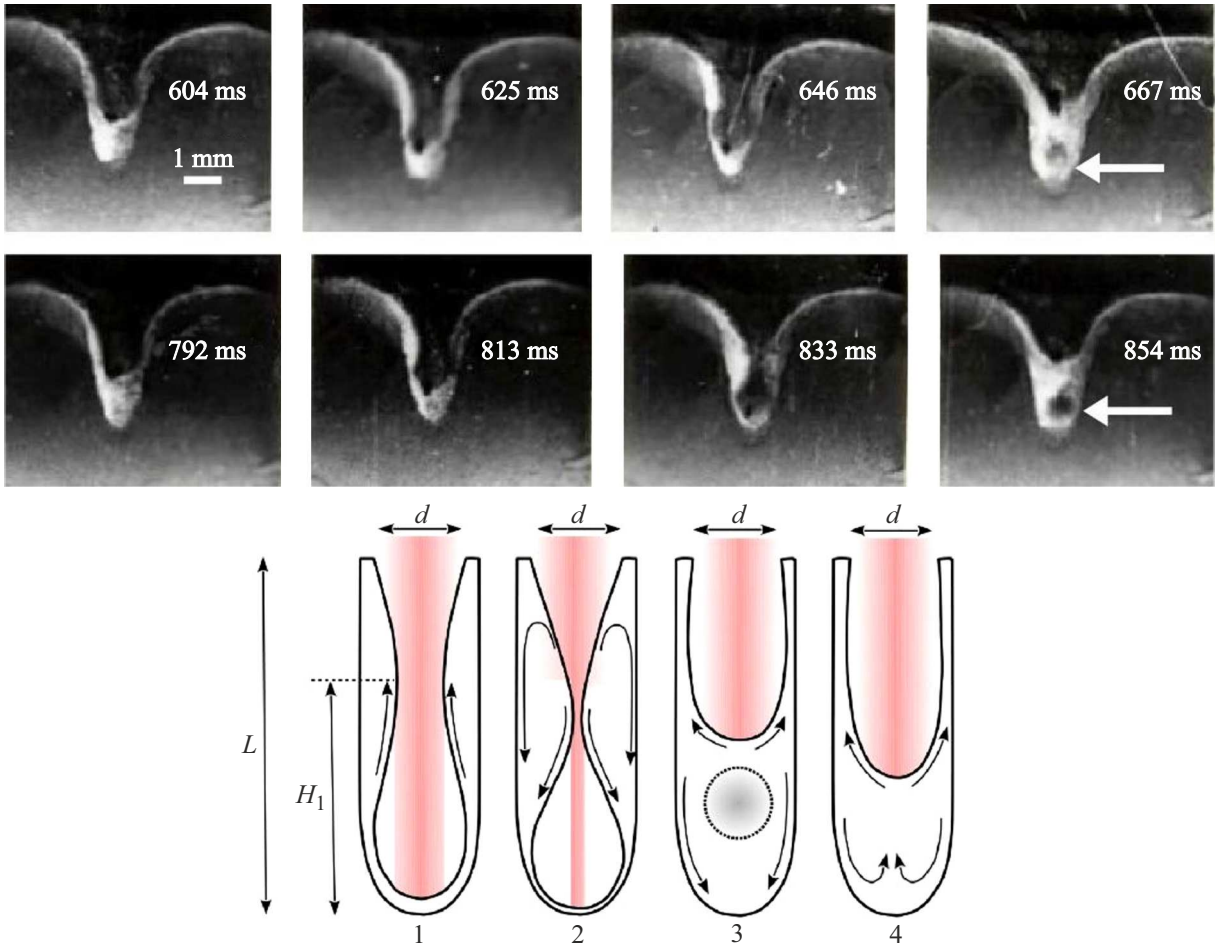

Figure 8. Photographic images and diagram of capillary-wave oscillations of the melt in a keyhole in paraffin with the capture of a gas bubble [25-27].

possible rapid keyhole collapse at the 3rd stage of evolution. Presumably, the sudden „loss“ of the tracked object made it difficult to interpret the causes. With the experimental data from [45] (Section 5, Fig. 7) taken into account, one may assume that this termination of evolution curve tracking is the result of a rapid keyhole collapse at the 3rd stage.

A similar difficulty is noted in experiments [49] on reconstructing the keyhole evolution in stainless steel under the influence of a laser pulse with a rising front (Fig. 10). The results revealed a sharp discontinuity dividing the keyhole evolution curve into two sections L_1 and L_2. Section L_1 represents the 1st stage of keyhole formation with its two clearly distinguishable phases (slow melting and rapid keyhole growth) and a very short 2nd stage of evolution, which consists of just one oscillatory cycle. This is followed by a sharp discontinuity at the moment of reaching the maximum energy in a pulse; the continuation of the evolution curve is denoted as L_2 (the dotted curve in Fig. 10). Just as in [43], the authors made no comment on this discontinuity in keyhole evolution, which is likely to be attributable to the same difficulty in interpreting the rapid keyhole collapse.

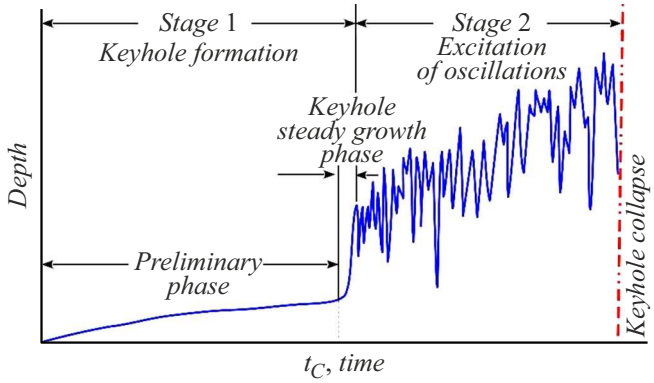

Figure 9. Analysis of the keyhole evolution in a titanium alloy under the point impact of laser radiation (based on the experimental data reported in [43]).

The photographic images of cross sections of the melting zone with traces of crystallization of spiral flows from the drain funnel formed during the collapse in region L_2 (Fig. 10), which were presented in [49], provide an insight

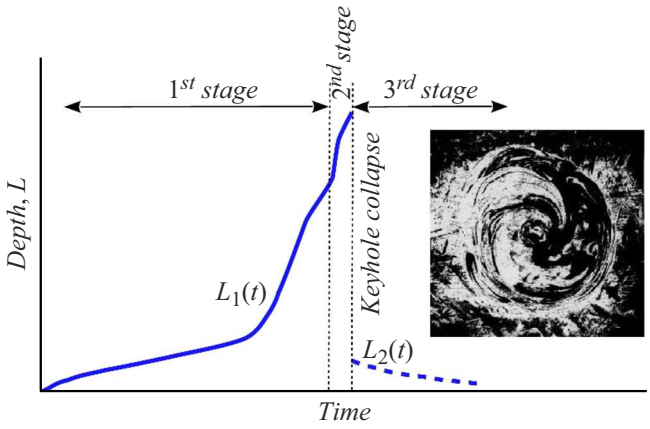

Figure 10. Analysis of the experimental data from [49]. Keyhole evolution in stainless steel under the point impact of a laser pulse with a rising front. Cross section with traces of spiral melt flows in the keyhole throat.

into the collapse mechanism. The spiral nature of flows explains why the darkening wave moves from right to left (similar to a shutter) in frontal video recording in [19,45] and why the keyhole images vanish instantaneously and entirely in experiments [43]. With such „loss" of the tracked object, this stage of the keyhole evolution cannot be represented by a continuous $L(t)$ curve. Therefore, curve $L(t)$ is simply interrupted in [43] and plotted in two parts with a discontinuity in [49]; in [47] (Fig. 7), the interruption of $L(t)$ is combined with a shaded region.

7. Evaluation of the relative contributions of mechanisms in deep penetration of metals

We use the Bernoulli equation for an ideal liquid (the viscosity of liquid metals is low) to estimate the contribution of the ablation mechanism to melt transfer. When the ablation mechanism is dominant, the balance of static pressures in liquid is given by

$$\frac{\sigma}{R} + \rho g z = p_{ABL}, \qquad (3)$$

where p_{ABL} is the ablation vapor pressure, σ/R is the Laplace pressure, $\rho g z$ is the hydrostatic pressure, R is the surface curvature radius, g is the gravitational constant, and z is the coordinate along the beam axis. Let us use the experimental data from [11] on melting of Armco iron with a 7.2 kW electron beam in vacuum to evaluate the terms of Eq. (3). Penetration depth $L = 20$ mm was achieved with aspect ratio $L/D = 8$. The mentioned experiment is unique in its set of measurements, which includes the surface tension of liquid iron ($\sigma = 0.42\,\mathrm{J/m^2}$) and the pressure in the keyhole ($p_{ABL} = 0.31\,\mathrm{kN/m^2}$) and provides an opportunity to evaluate each term of Eq. (3).

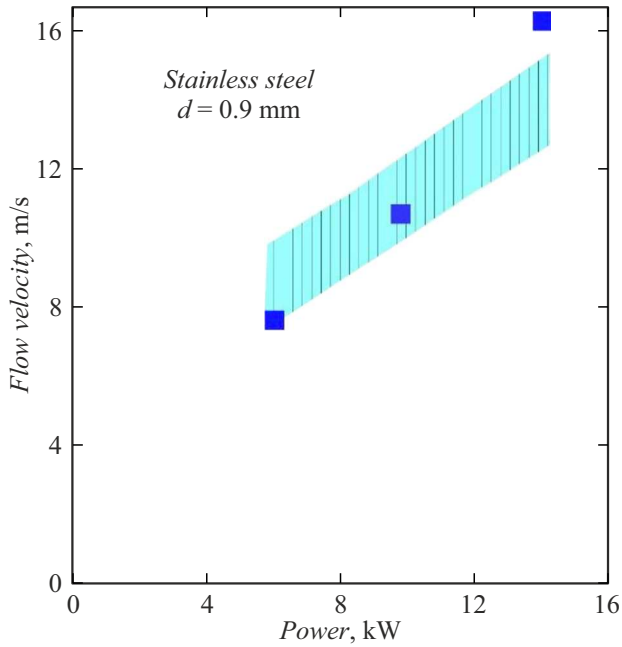

Figure 11. Variation of melt flow velocity with increasing laser power. Points and the shaded region represent the experimental data [50] and the results of calculation according to relations (1) and (2).

1) The Laplace pressure is $\sigma/R \approx 3.6-4.2\,\mathrm{kN/m^2}$ at measured surface tension $\sigma = 0.42\,\mathrm{J/m^2}$ and keyhole radius $r \approx 1.0-1.15$ mm (with account for molten zone diameter $D \approx 2.5$ mm at known values of $L = 20$ mm and $L/D = 8$).

2) The hydrostatic pressure is $\rho g L \approx 2\,\mathrm{kN/m^2}$.

3) The measured vapor pressure in the keyhole is $p_{ABL} = 0.31\,\mathrm{kN/m^2}$.

It follows from a comparison of pressure values that the measured pressure in the keyhole is an order of magnitude lower than the sum of Laplace and hydrostatic pressures; therefore, it cannot provide mechanical support for the keyhole. This excludes the possibility that the ablation mechanism is dominant.

Measurements of the melt flow velocity at the front wall of the keyhole in stainless steel [50] provided another opportunity to estimate the contribution of ablation pressure. With a laser radiation focusing spot diameter $d = 0.9$ mm and a laser power of 6, 10b and 14 kW, the average values of melt velocity V were 7.5, 10.77, and 16.24 m/s, respectively (Fig. 11, Table 1 (Nos. 1 and 2)). The corresponding calculated values of TC flow velocity are shown in Fig. 11 (owing to the spread of values of stainless steel parameters, velocities are presented in the form of a shaded region) and in Table 1 (No. 3). Notably, the calculations agree closely with the measurement data.

The ablation vapor pressure is spent not only on mechanical support of the keyhole, but also on melt removal from the irradiation zone at significant rates (see above).

Table 1. Analysis of the DP mode parameters based on the experimental results [50]

№	Parameters	Experimental conditions [50]			Experiments
1	Laser power, kW	6	10	14	
	Focal spot diameter, mm	0.9			
2	Melt velocity at the front wall of the keyhole (experimental points in Fig. 11), m/s	7.5	10.77	16.24	
Thermocapillary mechanism (calculation)					
3	Thermocapillary melt flow velocity (calculation region in Fig. 11), m/s	7.7−10	10−13	12−15.5	
Ablation mechanism (calculation)					
4	Ablation vapor pressure in the keyhole, kN/m^2	225	460	1055	~ 0.31 [11]
5	Vapor outflow rate, m/s	475	670	1058	10−50 [52,53]
6	Rate of mass loss due to evaporation, mg/s	350	540	790	2−8 [51,54]
7	Laser power spent on evaporation, kW	2.191	3.373	4.914	
	Percentage of laser power spent on evaporation, %	36	34	35	0.5−0.6 [55]

Therefore, the sum of static pressures in Eq. (3) should be supplemented with dynamic flow pressure $\rho V^2/2$:

$$\frac{\sigma}{R} + \rho g z + \frac{\rho V^2}{2} = p_{ABL}. \quad (4)$$

Ablation pressure p_{ABL} may be expressed in terms of measured rate of mass loss m/t from focal spot area S. The rate of lowering of the melt level due to mass loss is then $V_{ABL} = \frac{m}{St\rho}$. Using the condition of conservation of mass flow rate $\rho_V V_V = \rho V_{ABL}$ (ρ_V, V_V are the density and velocity of vapor flow), we write the following for recoil vapor pressure:

$$p_{ABL} = \rho_V V_V^2 = \rho V_{ABL} V_V = \frac{m V_V}{St}. \quad (5)$$

Taking (5) into account, one may rewrite Eq. (4) in measurable quantities:

$$\frac{\sigma}{R} + \rho g z + \frac{\rho V^2}{2} = \frac{m V_V}{St}. \quad (6)$$

The dynamic pressure estimate corresponding to the measured values of flow velocity $V = 7.5-16$ m/s [50] is $\rho V^2 \approx 225-1055$ kN/m^2. Taking $\rho_V \sim 1$ kg/m^3 [51] into account, we estimate the vapor outflow rate at $V_V = \sqrt{\frac{p_{ABL}}{\rho_V}} \sim 475-1058$ m/s (Table 1, No. 5), which is 1.5−2 orders of magnitude higher than the values normally observed in experiments (10−50 m/s [52,53]).

Let us estimate the power cost of evaporation. According to (5), the rate of mass loss in vapor needed to support mechanically a keyhole with a diameter of ~ 1 mm by vapor pressure should be estimated at $\frac{m}{t} = \rho S V_{ABL} = \frac{\rho V_{ABL} \pi d^2}{4} = 350$, 540, and 790 mg/s (Table 1, No. 6) with a beam power of 6, 10, and 14 kW, respectively. However, such m/t values are 1.5−2 orders of magnitude higher than the typical experimental values of $\sim 2-8$ mg/s [51,54]. In addition, high rates of mass loss m/t should correspond to high levels of laser power consumption for evaporation $(m/t)H_V = 2.19$, 3.373, and 4.914 kW (H_V is the specific heat of evaporation) at a laser power of 6, 10, and 14 kW, respectively (Table 1, No. 7). These consumption figures amount to 34 %−36 % of the total laser power and are 2 orders of magnitude higher than the actual values (~ 0.5 %−0.6 %) confirmed by experimental measurements [55] performed for stainless steel and a welding laser power of 10 kW. Note that anomalously high evaporation costs (~ 40 % of the laser power) were also obtained in the calculation example with the ablation mechanism, which was presented in Section 4.1 of monographs [2,38].

A low level of excess vapor pressure in the keyhole was also confirmed by measurements during welding in vacuum. For example, it was as low as 19−570 Pa [10] when Al alloys were welded with an electron beam with a power of 1.1−3.85 kW, and was measured at 436 and 404 Pa when Armco iron and titanium alloy VT1-0, respectively, were subjected to electron-beam welding [12]. In addition, a low vapor pressure ($\sim 10^2$ Pa) in the keyhole was noted in [56] with reference to measurements [57]. In [58], the conclusion regarding a low pressure in the keyhole during welding with a 25 kW laser beam was formulated on the basis of detection of protective gases (Ar, He) in the pore volume [59]. The authors of [60] did also note that air or protective gas (depending on the composition of the working medium) were found in the pore volume. All these data call into question the dominance of the ablation mechanism in the DP mode. No measurements of pressure

in the keyhole indicative of a high excess vapor pressure ($\sim 10^3-10^5$ Pa) needed for the ablation mechanism were found.

8. Threshold transition to the DP mode

Estimates of the threshold conditions for transition to the DP mode based on the assumed dominance of the ablation mechanism should rely on the magnitude of surface deformation due to a sharp increase in recoil vapor pressure observed when a certain temperature of developed evaporation T^* is reached [44]. Apparently, the first analytical expression for threshold power density of the transition to the DP mode was obtained in [61] with the use of fitted parameters. This approach provided nothing beyond rough estimates and was not developed further.

Models of the DP mode have long incorporated the assumption of saturation of heating of the keyhole walls at boiling point T_B, which was later confirmed by measurements [39]. It is believed that the sharp exponential increase in ablation vapor pressure at boiling point T_B is the cause of keyhole formation. Thus, boiling point T_B and developed evaporation temperature T^* are assumed to be equal, which is inconsistent with the results of numerical calculations of temperature on the keyhole walls. For example, according to calculations [31], deep penetration of stainless steel under the influence of high ablation pressure requires heating the keyhole walls to temperatures of $\sim 4000-4200$ K, which are significantly higher than $T_B \sim 3300$ K.

The temperature criterion for threshold transition to the DP mode at $T = T_B$ is often used to obtain an order-of-magnitude estimate of threshold switching of melting modes. For example, this criterion was used in [62,63] in the analytical expression for the dependence of threshold power on spot diameter d and beam scan rate W and in [64,65] to identify the threshold transition by examining the combined effects of power, scan rate, and size of the beam. Notably, negligible energy losses due to evaporation were assumed in this case, which excludes the possibility that the ablation mechanism is dominant in supporting a steady cavity (as was demonstrated in Section 7, this requires $\sim 30\%-40\%$ of the absorbed laser power, and such power consumption cannot be neglected). Note that temperature criterion $T = T_B$ and the assumption of low energy losses due to evaporation agree closely with the TC mechanism of formation of the DP keyhole.

The threshold condition for melting mode change may be determined using the TC mechanism if dependence (2) for the thickness of shear TC flow $h = \delta$ is applied in the heat flux density equation (Fourier law). The dependence of absorbed threshold power on focal spot size d then takes the form

$$AP_{th} = \frac{Aq_{th}(d)\pi d^2}{4} = \frac{\lambda(T_B - T_M)\pi d^2}{4\delta} = \frac{\pi\lambda\{d(T_B - T_M)\}^{4/3}(\rho\sigma_T^2/\chi)^{1/6}}{4\eta^{1/2}}. \quad (7)$$

Here, A is the effective absorption of radiation by the keyhole, which reaches a level of $A = 0.6-0.9$ [40,41] in the DP mode due to multiple reflections (see Fig. 3).

Figures 12, 13 present a comparison of dependence $AP_{th}(d)$ (7) of the absorbed threshold power with effective absorption within the $A = 0.5-1$ range with experimental data for the main structural metals Fe, Cu, Al, and Ti (Table 2). This comparison reveals quantitative and qualitative agreement between the calculated results and experimental data over a wide range of d variation. The $AP_{th} \sim d^{4/3}$ nature of the dependence is confirmed. Therefore, a correct characterization of threshold conditions for each metal should include not only the power (or power density), but also the focal spot size.

In Figs. 12 and 13, formula (7) is compared with the analytical dependence of threshold power for a round focal spot with a uniform power distribution proposed in [63]. Calculations were performed for Fe, Cu, Al, and Ti with the spot diameter values varying within a wide range typical of laser welding and the additive process of selective laser melting of powder layers. Calculations in accordance with the formula proposed in [63] were performed for two beam scan rates $W = 0$ and 1 m/s, which are shown in gray. A total of 36 experimental points obtained in 25 studies were used for comparison. The scatter of experimental data is within the limits of possible variation of effective absorption $A = 0.5-1$.

The comparison demonstrates that relation (7) characterizes the threshold conditions much more accurately than the formula proposed in [63]. A sufficient closeness of agreement between the calculations using relation (7) and the experimental data verifies the correctness of the initial assumptions regarding the causes of threshold transition to the DP mode. The confirmed accuracy of expression (2) for the thickness of shear TC flow allows one to formulate requirements as to the computational grid step in numerical models of the DP mode.

The dependence of threshold power on the absorption of radiation with different wavelengths is illustrated by the results for copper (points Cu 2 and 3) [72] obtained under the influence of laser radiation with a wavelength of 515 and 1030 nm. In this case, the absorption of radiation by a flat copper surface within the green range of the spectrum (515 nm) is close to 0.4, while the approximate absorption of IR radiation (1030 nm) is 0.03. However, the effective absorption increases as a result of multiple reflections in the keyhole. The value of A for green radiation (515 nm) and IR radiation is close to unity and the $A = 0.5$ limit, respectively.

The ingression of cold metal onto the beam at a high scan rates interferes with propagation of the melting boundary on the front keyhole wall and reduces the thickness of the molten layer. This is what shapes the dependence of threshold power on the scan rate. The increase in threshold power with increasing scan rate is reflected in the experimental results (points Fe 2,3,4) [40] for stainless steel obtained at a scan rate of $W = 100$, 500, and 1500 mm/s.

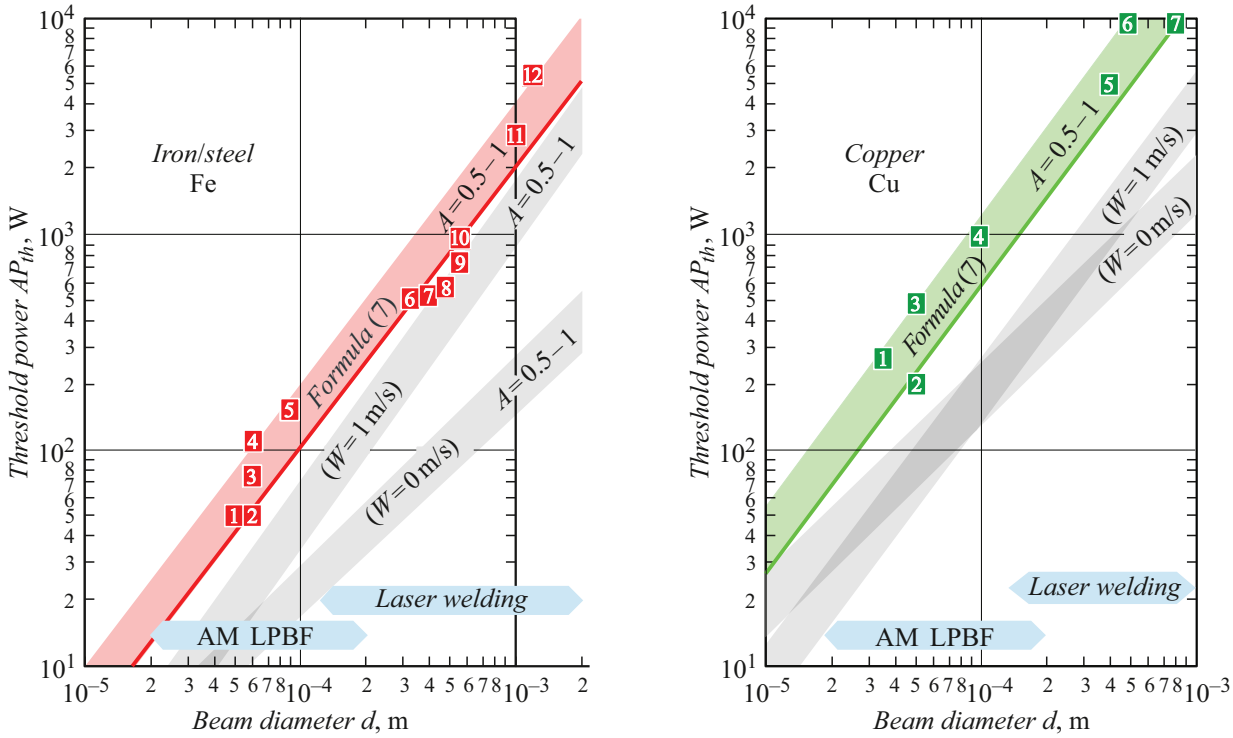

Figure 12. Variation of threshold power of melting mode change for Fe and Cu with size of the focal spot: comparison of formula (7) with the relation proposed in [63]. Points represent the experimental data (Table 2).

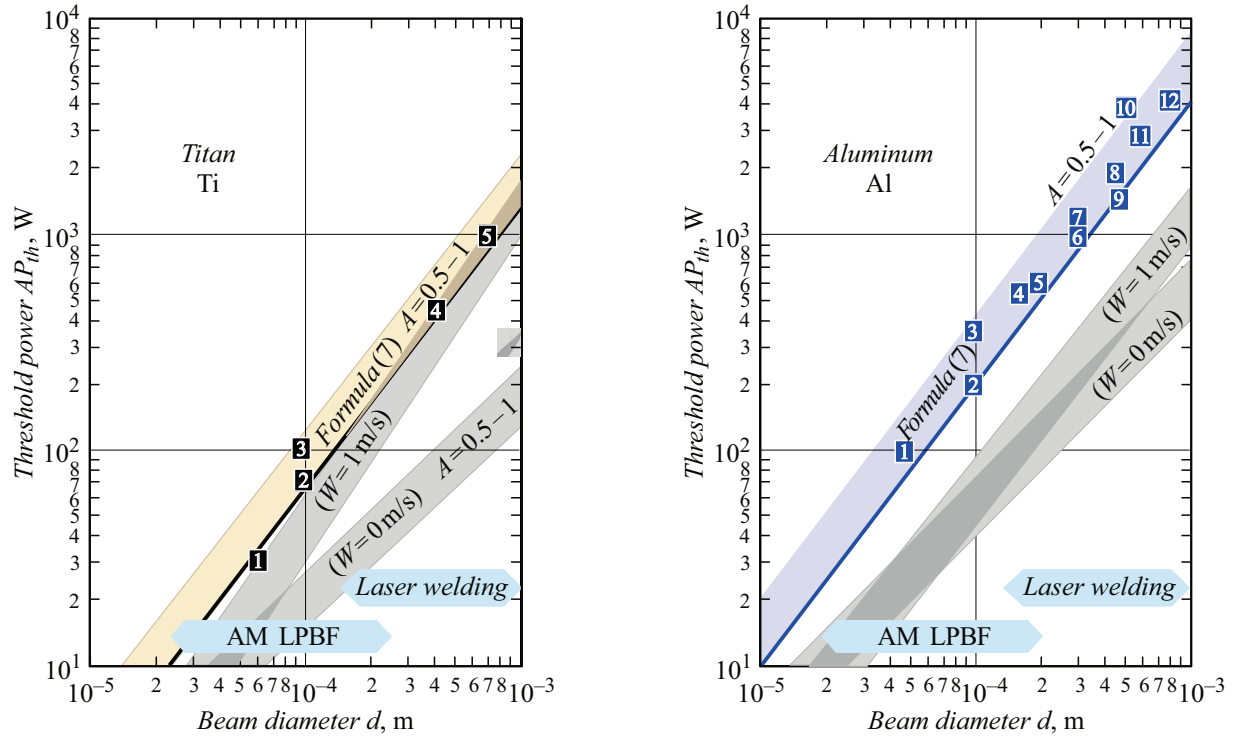

Figure 13. Variation of threshold power of melting mode change for Ti and Al with size of the focal spot: comparison of formula (7) with the relation proposed in [63]. Points represent the experimental data (Table 2).

Table 2. Correspondence between the point numbers in Figs. 12 and 13 and experimental studies from the list of references

Iron (steel)	Point No.	1	2,3,4	5	6	7,9,12	8	10	11
	Experiment	[68]	[40]	[67]	[46]	[4]	[68]	[69]	[70]
Copper	Point No.	1	2,3	4	5	6	7		
	Experiment	[71]	[72]	[73]	[74]	[75]	[76]		
Titanium	Point No.	1	2	3,4	5				
	Experiment	[77]	[78]	[43]	[79]				
Aluminum	Point No.	1	2	3–6,8,11	7	9	10	12	
	Experiment	[66]	[80]	[81]	[82]	[83]	[84]	[6]	

9. Requirements as to discretization of the computational domain and time in numerical modeling of the DP mode

It is known that the veracity of a numerical solution is affected not only by the completeness of the system of equations and boundary conditions characterizing the model, but also by the correspondence of the chosen step of the computational grid and the time step to the real scale of the physical process. In addition to inclusion of the boundary condition for the action of TC forces on the melt surface and precise determination of the position of the melting front at the front wall, correct reproduction of shear TC flow with thickness $h = \delta$ requires a physically justified choice of step Δx of the computational grid to ensure the required „resolution" of the model. The grid step should be significantly (∼an order of magnitude) smaller than scale $\delta = h$; i.e., $\Delta x \leq 0.1h$. Time step Δt should be related to Δx and the TC flow velocity by Courant–Friedrichs–Lewy (CFL) criterion $\Delta t \leq \Delta x/V$, where V is determined in accordance with (1).

Let us consider scales $h = \delta$ and V and the technological range of laser power, the lower limit of which is set by threshold condition (7). Table 3 lists the calculated estimates of $AP_{th}(d)$ for two values of d differing by an order of magnitude that are typical of laser welding ($d = 500\,\mu$m) and the additive process of selective laser melting ($d = 50\,\mu$m). The technological range is bounded from above by the need to comply with quality standards (e.g., the onset of unwanted splashing and droplet dispersion). Under typical iron welding conditions, this occurs at $q_{spl} \sim 3\,\text{MW/cm}^2$ [5], which is ~ 7.5 times higher than threshold value $q_{th} = 0.4\,\text{MW/cm}^2$ (at $d = 500\,\mu$m) [4]. Thus, the technological range may be characterized approximately by ratio $q_{spl}/q_{th} \sim 7.5$. If we assume that quantity q_{spl}/q_{th} is conserved when d changes, the approximate estimate of the upper boundary of the technological interval for $d = 50\,\mu$m and the corresponding threshold value $q_{th} = 1.9\,\text{MW/cm}^2$ is $q_{spl} \sim 14\,\text{MW/cm}^2$. The variations of thickness of shear TC flow ($h = \delta$) in iron and its velocity V within the $q_{spl}/q_{th} \sim 7.5$ technological range (at $d = 50$ and $500\,\mu$m) are presented in Fig. 14 and Table 3.

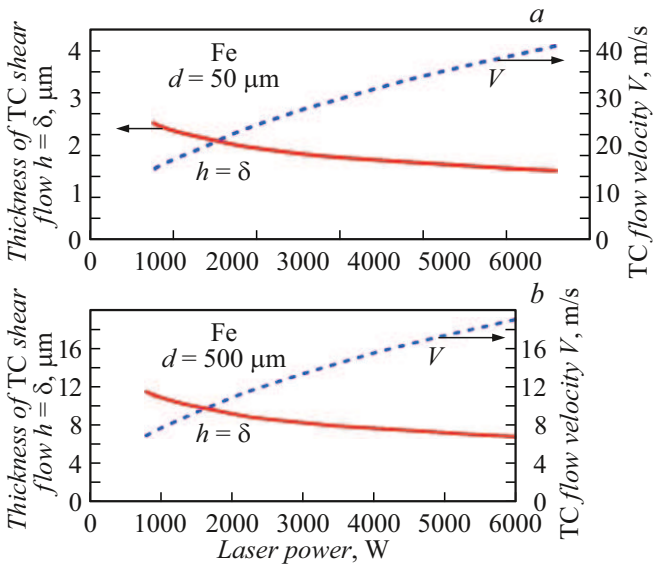

Figure 14. Power dependences of thickness of the shear TC layer ($h = \delta$) and TC flow velocity during the formation of a cavity in iron calculated according to relations (2) and (1) with different radiation focusing, d: a — 50, b — 500 μm.

The calculated field within irradiation spot $d = 50\,\mu$m should have at least $d/\Delta x \geq 10d/h \sim 200–330$ nodes (or at least $\sim 420–720$ nodes at $d = 500\,\mu$m). According to the CFL criterion, the time step should satisfy condition $\Delta t \leq \Delta x/V$. The variations of $V(P)$ at two values of d are presented in Fig. 14 and Table 3. With these calculated data taken into account, the grid and time steps turn out to be within the nanometer and nanosecond ranges. Therefore, the solution requires considerable computational resources. For example, calculations [32], where the possibility of cavity formation with minor evaporation under the dominant influence of the TC mechanism was revealed, were performed using one of the top supercomputers in the world.

The presented technique allows one to analyze the correctness of discretization of the computational domain

Table 3. Parameters of discretization of the computational domain for the DP mode simulation in iron with two focal spot diameters d

Focal spot diameter d, μm	500	50
Threshold power AP_{th}, W (calculation)	800	37
Threshold power density Aq_{th}, MW/cm^2 (calculation)	0.4	1.9
Technological range of power density q, MW/cm^2 (estimated, $q_{spl}/q_{th} \approx 7.5$)	$0.4 \rightarrow 3$	$1.9 \rightarrow 14$
Shear flow thickness $h = \delta$ (calculation), μm	$11.5 \rightarrow 7$	$2.5 \rightarrow 1.5$
TC flow velocity V (calculation), m/s	$7 \rightarrow 19$	$15 \rightarrow 41$
Estimated grid step $\Delta x \sim 0.1 \sim h$, μm	$\leq 1.2 \rightarrow 0.7$	$\leq 0.25 \rightarrow 0.15$
Time step estimated in accordance with the CFL criterion $\Delta t \sim \Delta x/V$, ns	$\leq 170 \rightarrow 37$	$\leq 17 \rightarrow 3.7$

in those numerical models of the DP mode that contain information about the computational grid. Note that no physical justification is often provided for the choice of grid and time steps. The results are rarely tested for grid independence. The presented technique makes it possible to overcome these difficulties in assessing the correctness of resolution setting for each numerical model.

Let us illustrate the discretization analysis of computational models using the examples of six models with information about the computational grid available [28–31,85–87].

In [28,29], time step $\Delta t = 1\,\mu$s was used to model the penetration of steel by laser radiation with $d = 0.5$ mm. It follows from Table 3 that, according to the CFL criterion, the limit value of the time step at $d = 0.5$ mm should fall within the $\Delta t = 0.037{-}0.17\,\mu$s range. The mentioned step value of $\Delta t = 1\,\mu$s is too large to provide adequate reproduction of the TC mechanism. Indeed, the obtained values of flow velocity $V \sim 1{-}2$ m/s (with power $P = 4$ kW and $d = 0.5$ mm) are an order of magnitude lower than $V = 15.5$ m/s calculated under the same conditions according to relations (1) and (2).

The authors of [30] used a computational grid with a step of $20\,\mu$m to modeling laser penetration of steel ($d = 0.3$ mm). This value is an order of magnitude greater than $\Delta x \sim 0.1 \sim h = 0.82\,\mu$m ($h = \delta = 8.2\,\mu$m) recommended for proper reproduction of the TC mechanism. Therefore, it was impossible to reproduce TC flow in [30], and the conclusion regarding the supposedly insignificant (in comparison with the ablation mechanism) influence of Marangoni flow on the formation of a cavity is untenable.

Laser penetration of steel ($d = 0.5$ mm) was simulated in [31] using a non-uniform grid system of 202×252 points for a computational domain 5.0×6.25 mm in size (the average step is $\sim 25\,\mu$m). The minimum spatial grid step was not reported, but the minimum time step $\Delta t \sim 1\,\mu$s was indicated, which is an order of magnitude greater than the recommended values of $\Delta t \leq 0.17{-}0.037\,\mu$s (Table 3). Thus, the temporal and spatial discretization used in [31] is insufficient to support an accurate calculation.

Point penetration of the Inconel 625 alloy by a laser pulse with power $P = 700$ W focused into a spot $d = 205\,\mu$m ($q = 2.1$ MW/cm^2) was simulated in [85]. A spatial grid of triangular elements with a local step reduction to $2\,\mu$m was used. According to (2), the thickness of shear TC flow corresponds to $h = \delta \sim 5\,\mu$m; i.e., the minimum step of $2\,\mu$m used in calculations is only 2.5 times smaller than the thickness of TC flow, which is insufficient for its accurate numerical reproduction. The smallest time step used in the model was $1\,\mu$s, which is more than an order of magnitude larger than the recommended value. Indeed, it follows from (1) that the magnitude of TC flow velocity is $V = 13.4$ m/s, and the CFL criterion stipulates that the time step should not exceed $\Delta x/V = 0.037\,\mu$s. Consequently, the discretization used in [85] cannot ensure proper reproduction of TC flow.

The authors of [86] presented a computational fluid dynamics model of selective laser melting in the DP mode with simulation of an unstable cavity and pore formation. Calculations of stainless steel penetration were performed with grid step $\Delta x = 4\,\mu$m. At $d = 45\,\mu$m, the thickness of shear TC flow is $h = \delta \sim 2\,\mu$m; i.e., the recommended grid step is $\Delta x \sim 0.1h = 0.2\,\mu$m ($\sim 20$ times smaller than the used value of $\Delta x = 4\,\mu$m). Thus, the grid step used in [86] cannot provide accurate reproduction of shear TC flow at the front wall of the cavity.

A model of the additive process of selective laser melting of AISI H13 steel in the deep penetration mode with focusing of radiation into a spot with a diameter of $50\,\mu$m was presented in [87]. To determine the reliability of the numerical model and the appropriate grid size, grid convergence was analyzed with the size of computational cells varied from 3 to $10\,\mu$m. A grid step of $4.5\,\mu$m was chosen based on the results of these grid convergence studies. However, it follows from Table 3 that the thickness of TC flow at $d = 50\,\mu$m does not exceed $h = \delta \sim 2.5{-}1.5\,\mu$m, and the physically justified grid step is as small as $\Delta x \sim 0.1h = 0.25{-}0.15\,\mu$m. Therefore, the calculations in [87] were performed at a grid step

20–30 times greater than the recommended one and cannot provide a proper description of hydrodynamic processes.

The above examples illustrate a typical error of modern models of the DP mode: the use of a computational grid step that exceeds significantly the maximum permissible value for correct reproduction of shear TC flow. This error leads to an underestimation of contribution of the TC mechanism and an overestimation of contribution of the ablation mechanism and, consequently, to incorrect CAD engineering results.

10. Generation of pores by an unstable keyhole during beam scanning

It makes sense to divide the evolution of a keyhole under the influence of stationary continuous-wave radiation into three stages differing in the specific features of hydrodynamic processes (Sections 2, 6). With the beam scan rate being equal to W, the first two stages are confined within irradiation spot d and exposure time d/W. To maintain a deep keyhole, one needs to exclude the last (third) stage with flow-in and keyhole collapse. This may be achieved if the scan rate is not too slow and exposure time d/W is not too long. The ingression of cold metal onto the beam induces asymmetry of the keyhole, the formation of which (1st stage of evolution) corresponds to melting at the front wall. Oscillations in the keyhole (2nd stage) correspond to the processes at its root. They were characterized in [19,20,25–27] and lead to the generation of unwanted pores (Fig. 15), which act as stress concentrators and reduce significantly the service life of parts under dynamically changing loads. Such pores need to be eliminated in high-duty products, especially in those produced by additive manufacturing with selective melting of metal powders by a laser or electron beam, where the elimination of pores allows one to both maximize the density and enhance the strength due to the effect of steep temperature gradients and high crystallization rates, which contribute to grain refinement and alter the metal microstructure.

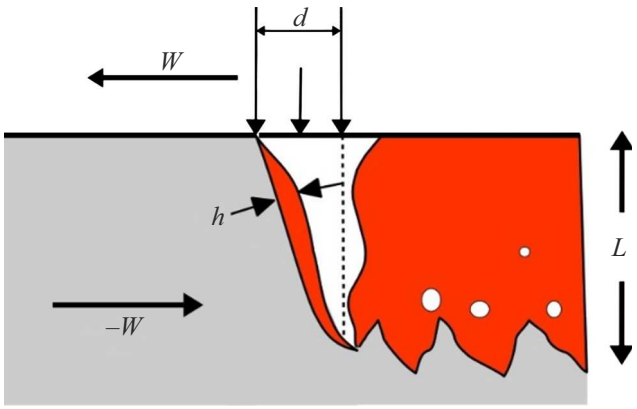

Figure 15. Oscillations of the molten layer in the keyhole lead to oscillations of its root part and pore formation.

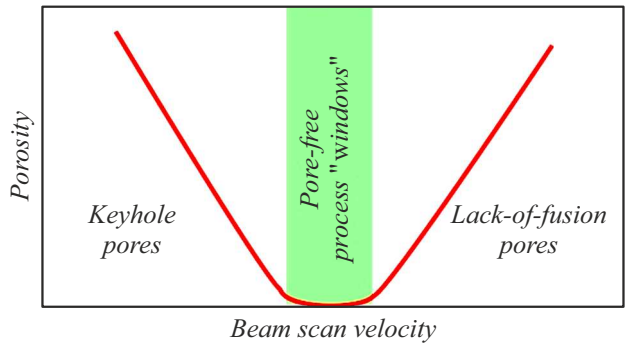

Figure 16. Typical trend of porosity variation with scan rate and technological „window“ free from pore formation.

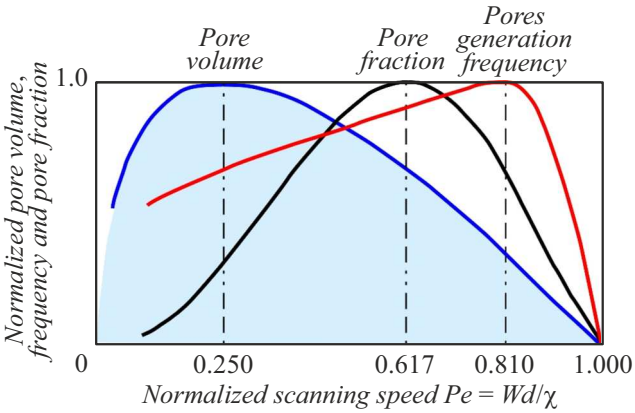

Figure 17. Effect of scan rate W on pore volume $Vol(W)$, pore generation frequency $f(W)$, and pore fraction $G(W)$ [26,27]. All quantities are normalized to their maximum values.

The development of process procedures suppressing the formation of pores is a complex problem. Solving it through trial and error requires about a hundred technological tests. These tests will take approximately a year and require significant effort, but their result is hard to predict. Attempts at reducing time and effort expenditure through numerical modeling have resulted in the publication of a large number of models, which, however, have not yet managed to reproduce the main trends in pore formation.

Beam scan rate W is believed to be the most important factor shaping the pore formation trends. As was noted in [88–90], the cause of emergence of pores at relatively low values of W is the keyhole instability (*keyhole pores*), while the lack of melt drives pore formation at high W values (*lack-of-fusion pores*) (Fig. 16). The process window with zero pore formation lies between these W intervals. Prediction of the position of the process window on the W axis is beneficial for process design (CAD engineering). The interpretation of the typical trend of porosity variation with W based on the generation of pores by excitation of capillary waves in the keyhole provided an opportunity to obtain dependences of pore formation parameters (pore volume, generation frequency, and fraction) on the scan

rate [26,27]. These dependences were verified by comparison with experimental data and are presented in normalized form in Fig. 17.

It was found that all porosity characteristics turn to zero at $W = \chi/d$ (or at Peclet number $Pe = Wd/\chi = 1$); i.e., the technological window condition is satisfied at $Pe = Wd/\chi = 1$. The positions of maxima of the pore characteristics on the axis of normalized scan rate $Pe = Wd/\chi$ variation were determined. Pore volume $Vol(W)$ and pore generation frequency $f(W)$ are maximized at $Pe = 0.25$ and $Pe = 0.81$, respectively. In practice, it is convenient to evaluate the pore content through density variation $G = 1 - \rho_0/\rho_n$, where ρ_0 is the measured density after melting and ρ_n is the nominal density. This porosity index is proportional to the product of pore volume and pore generation frequency ($G \sim f(W)Vol(W)$) and is maximized at $Pe = 0.617$.

Pore generation by capillary waves (*keyhole pores*) is feasible at a positive molten mass balance ($h(W) > 0$) when the scan rate speed corresponds to Peclet number $Pe = Wd/\chi < 1$ (or $W < \chi/d$). If rate W is high and corresponds to $Pe > 1$ (i.e., $W > \chi/d$), melt imbalance is observed at the root of the keyhole, which causes the emergence of voids due to a lack of melt (*lack-of-fusion pores*). Rate $W = \chi/d$ (or $Pe = 1$) corresponds to the technological window with zero pore formation (Fig. 16). It is fundamentally possible to predict its position with the required accuracy and use these data in process design (including digital CAD design).

11. Electrocapillary acceleration of TC melt flow during DP of metals

It was demonstrated above that the TC mechanism establishes a plausible connection between physical processes in the DP mode and hydrodynamic flow. At the same time, the TC mechanism does not reveal the nature of the synergistic effect in hybrid laser-arc processing [34] and the reason behind the empirically observed correlations of the penetration depth with the ambient pressure, the characteristics of near-surface plasma, the emission current signal [35], and the direction and strength of the external electric field [36]. In our view, the probable acceleration of flow by electrocapillary (EC) forces, which are induced by dependence $\sigma(\varphi)$ of surface tension on electric potential that is distributed non-uniformly along the surface, may fill this gap. The basic concepts regarding the physical mechanism of EC acceleration of melting in the process of DP of metals by high-power laser radiation were formulated in [37].

The transition to the DP mode is accompanied by the emergence of laser-induced plasma at the irradiation spot and the melt–plasma contact with the formation of a double electric layer (DEL). Owing to the locality of laser action, this induces non-uniform distributions of electric charge and potential on the melt surface that cause the EC effect

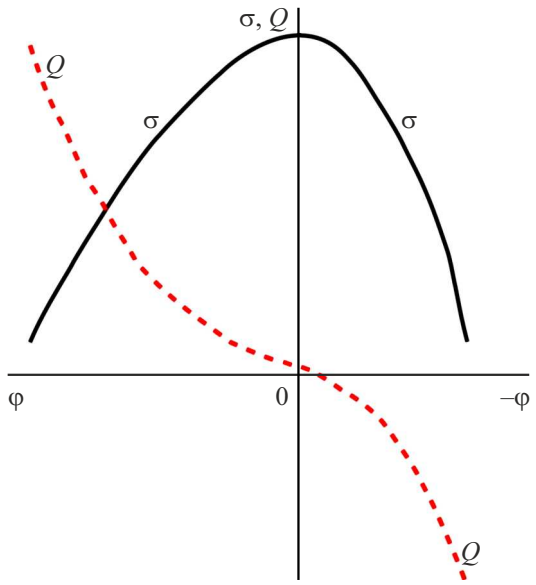

Figure 18. Typical EC curve $\sigma(\varphi)$ and variation of specific charge $Q(\varphi)$.

(due to dependence $\sigma(\varphi)$ of surface tension on electric potential) and result in the emergence of tangential EC forces. The formation of plasma and a DEL is facilitated by thermionic processes. Thermionic emission is characterized by current density given by the Richardson–Dushman formula $j_e = A_R T^2 \exp(-\omega/kT)$, where ω is the electron work function for the melt surface, k is the Boltzmann constant, and A_R is the thermionic constant. The emission current for iron ($\omega = 4.31$ eV) at a boiling temperature characteristic of the DP mode is $j_e = 0.33$ A/mm^2. Owing to the loss of electrons, positive charges are induced on the surface from the melt side, which trap electrostatically a certain fraction of electrons above the surface, establishing DEL charge separation. The DEL electric field counteracts the release of electrons from the melt surface and stimulates the emission of positive ions with a current density given by the Richardson–Smith formula $j_i = A_P T^2 \exp(-\omega_P/kT)$, where A_P is a constant and ω_P is the positive ion work function for emission from the melt. The combined thermionic emission of electrons and positive ions produces a total emission current equal to the sum of oppositely directed emission currents of electrons and ions: $J = S \cdot j = S(j_e - j_i)$, where S is the irradiation spot area. Total current J is zero at $j_e = j_i$ and specific charge $Q = 0$, which corresponds to the EC curve maximum (see Fig. 18).

The application of an external electric field with strength E alters the potential barrier of electron release and the emission current density in accordance with the Richardson–Dushman formula with the Schottky correction $j_e = A_R T^2 \exp[-(\omega - \Delta\omega)/kT]$, where $\Delta\omega = e(eE/4\pi\varepsilon_0)^{1/2}$ is the Schottky correction, e is the electron charge, and $\varepsilon_0 = 8.85 \cdot 10^{-12}$ F/m is the permittivity of vacuum. If field E is codirectional with the DEL field,

a higher potential barrier of electron release translates into a reduction in j_e. This facilitates the emission of positive ions and raises ion current density j_i. External field E enhancing the DEL field should induce concentration of negative charge on the surface (from the melt side). If the DEL field is weakened by external field E, positive charge should concentrate on the melt surface. Thus, the external field allows one to control the charge on the molten metal surface, which may be used to control the EC effect and hydrodynamic processes in the DP mode.

Let us consider the EC effect as flows induced by the surface tension σ gradient. Dependence $\sigma(\varphi)$ is represented by the EC curve with a maximum at $\partial\sigma/\partial\varphi = 0$ with a zero charge potential, which corresponds to zero total current $J = S \cdot j = S(j_e - j_i) = 0$ (Fig. 18). In the right branch of the EC curve, $\varphi < 0$ and $\partial\sigma/\partial\varphi > 0$ holds. The left branch ($\varphi > 0$) corresponds to $\partial\sigma/\partial\varphi < 0$. Lippmann equation $\partial\sigma/\partial\varphi = -Q$, which is known from the theory of EC phenomena, establishes the relation between the slope of the EC curve and charge Q per unit surface area for a given potential φ taken with the opposite sign. The right and left branches of the EC curve have $Q < 0$ and $Q > 0$, respectively. The dependence of penetration depth on the change in polarity of E (sign of Q) may then reflect the asymmetry of the EC curve relative to axis σ ($\varphi = 0$) with condition $|\partial\sigma/\partial\varphi|_{\varphi,Q>0} < |\partial\sigma/\partial\varphi|_{\varphi,Q<0}$ for its two branches.

Any increase in charge density (positive or negative) will result in a reduction in surface tension. This behavior is attributable to the fact that all charges at the interface act on each other with Coulomb repulsive forces directed tangentially to the free surface. Therefore, a smaller amount of energy is needed to expand the interface, which translates into a reduction in surface tension with an increase in potential.

When metals are exposed to focused laser radiation in the DP mode, the temperature and electric potential at the irradiation spot should vary along the metal surface, decreasing from their maxima in the center of the spot to zero at the periphery ($(\partial T/\partial r < 0,\ \partial\varphi/\partial r < 0)$). The surface tension will, in contrast, increase in this case, since $\partial\sigma/\partial T < 0,\ \partial\sigma/\partial\varphi < 0$. EC flows arise in addition to TC ones due to the presence of an unbalanced tangential gradient of surface tension induced by the tangential gradient of voltage, which, in turn, is induced by a non-zero tangential electric field component. In the general case, variables T and φ are dependent, although their interrelation has not been established yet. To simplify the problem, we consider the special case of independent variables T and φ. The balance of forces on the surface is then written as

$$\eta \frac{\partial V_r}{\partial z} = -\frac{\partial \sigma(T,\varphi)}{\partial r} = -\frac{\partial \sigma}{\partial T}\frac{\partial T}{\partial r} - \frac{\partial \sigma}{\partial \varphi}\frac{\partial \varphi}{\partial r}, \qquad (8)$$

where $-\partial\sigma/\partial T = \gamma > 0$ — temperature coefficient of surface tension, η is the dynamic viscosity, V_r is the tangential melt flow velocity, and r and z are the coordinates tangential and normal to the surface. Since the thermally and electrically induced terms $(\partial\sigma/\partial T)$ $(\partial T/\partial r)$ and $(\partial\sigma/\partial\varphi)$ $(\partial\varphi/\partial r)$ have the same signs in balance (8), the EC forces are always (regardless of the sign of Q) accelerating TC flow. Taking the fact that $\partial\sigma/\partial\varphi = -Q$ and $\partial\varphi/\partial r = -E_T$ into account, we rewrite (8) in the form

$$\eta \frac{\partial V_r}{\partial z} = \gamma \frac{\partial T}{\partial r} - QE_T. \qquad (9)$$

According to Gauss's law, the surface density of charge Q is related to the normal component of electric field strength E_Z as $Q = 2\varepsilon_0 E_z = 2\varepsilon_0(E_N + E_D)$, where E_N and E_D are the normal components of the external field and the DEL field, respectively (it is assumed that E_N, $E_D = \text{const}$). Tangential field component E_T is determined by the potential difference with maximum $\varphi_{\max}$ in the center of the irradiation spot with diameter d and a zero value ($\varphi = 0$) at the periphery. The estimate for E_T is $E_T \approx -2\varphi_{\max}/d$. Equation (9) then takes the form

$$\eta \frac{\partial V_r}{\partial z} \cong \gamma \frac{T_B - T_M}{d} + 4\varepsilon_0(E_N + E_D)\frac{\varphi_{\max}}{d}. \qquad (10)$$

The following estimate of velocity of thermally and electrically induced shear flow (characteristic of the DP mode) with a viscous sublayer with thickness $\delta < d$ is obtained from (10):

$$V_r \cong \frac{\delta}{\eta d}\{\gamma(T_B - T_M) + 4\varepsilon_0(E_N + E_D)\varphi_{\max}\}. \qquad (11)$$

Formula (11) establishes the relation between thermionic, electrocapillary, and hydrodynamic processes in the DP mode. According to (11), the electrodynamic characteristics at the metal–plasma interface affect the acceleration of TC melt flow at the irradiation spot and, consequently, the penetration depth enhancement. In the DP mode, the estimated TC flow velocity at $d = 0.5$ mm and characteristic values of $\delta \sim 10\,\mu$m is $V_r \sim 10$ m/s [50]. The flow velocity may increase by the same amount due to the EC effect if the TC and EC components in (11) are commensurate. This is confirmed indirectly by an 85 % increase in depth of steel penetration by laser radiation observed in [36] after the application of an external electric field. According to (10) and (11), the TC and EC effects are commensurate when $4\varepsilon_0(E_N + E_D)\varphi_{\max} \approx \gamma(T_B - T_M)$. With an estimate of $\gamma(T_B - T_M) \approx (0.2{-}0.6)V/m$ for structural metals, the approximate condition of commensurability of effects is $(E_N + E_D)\varphi_{\max} \approx \gamma(T_B - T_M)/4\varepsilon_0 \approx 10^{10}$ V^2/m.

According to (11), the mechanism of correlation of the penetration depth with the characteristics of near-surface plasma and the emission current signal [35] may be regarded as a result of changes in the velocity of EC flow with fluctuations in the DEL field and the maximum value of the electric potential on the surface of molten metal.

It should be noted that the total current in the electron-beam irradiation zone includes both total emission current $S \cdot (j_e - j_i)$ and system current $S \cdot j_b$: $J = S \cdot j = S \cdot (j_e - j_i - j_b)$. A high electron-beam system

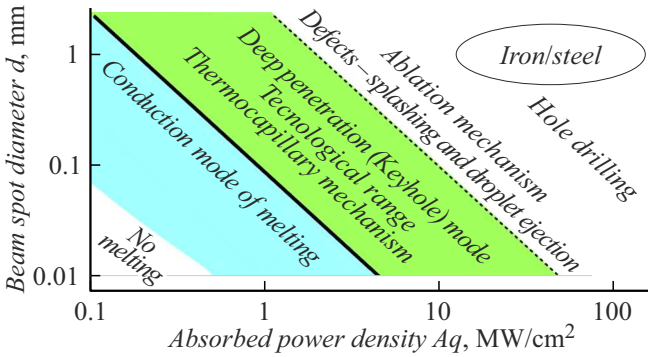

Figure 19. Diagram of hydrodynamic dissipation mechanisms changing sequentially with increasing power density supplied to iron (steel).

current $S \cdot j_b > S\ (j_e - j_i)$ provides an additional flow of negative charge to the metal surface, facilitating effective EC acceleration of hydrodynamic flows and increasing the penetration depth. An arc discharge in hybrid laser-arc processing has a similar effect on the surface charge density, which may be the cause of the synergistic melting effect [34] (i.e., violation of additivity of thermal effects of irradiation and arc discharge on a metal). In this case, the energy spent on melting may be more than 2 times greater than the sum of the corresponding energies released in the metal processed with each heat source individually (with a corresponding increase in processing efficiency). The presented mechanism allows one to formulate a physical interpretation of the experimentally observed correlations of the DP characteristics with thermionic and electrocapillary phenomena and indicates the direction of further research into the improvement and modeling of laser technological processes.

Conclusion

Let us formulate the most important issues and conclusions that we had no chance to discuss in more detail and that, in our opinion, must be taken into account in further research into technological processes, the development of production techniques, the simulation of the DP mode, and the validation of models.

It follows from the presented comprehensive analysis of experiments that, contrary to what is commonly believed and implemented in calculation models, the removal of melt from the irradiation zone is governed by the TC mechanism with a slight influence of the ablation mechanism. The dissipation of power entering the metal is effected by the hydrodynamic flow of melt. As the power increases, this dissipation is driven by hydrodynamic mechanisms changing in a strictly defined sequence. This sequence of mechanisms for iron (steel) is shown schematically in Fig. 19.

Their interchange is caused by a change in dissipation: the transition from TC convection, which is characteristic of the conduction melting mode, to TC formation of a keyhole due to an increase in TC flow velocity. With a further increase in power and evaporation, the contribution of the ablation mechanism becomes predominant outside the technological range. The presented sequence of dissipation mechanisms is often distorted in computer calculations, which is the probable reason why they fail to reproduce the hydrodynamic pattern. The distortion is attributable to the fact that the peculiarities of TC flow in the DP mode are neglected due to the use of an arbitrary and physically unjustified discretization of the region of formation of TC flow and time. Owing to their insufficient resolution, models do not „notice“ the TC flow and its influence on keyhole formation. As a result, the obtained results and conclusions are distorted, and the validation of models is extremely simplified.

A comprehensive analysis of the influence of hydrodynamic DP mechanisms inevitably leads to the conclusion that models need to be validated more thoroughly. Test computer visualization of the keyhole evolution under stationary irradiation may be used for this purpose. An adequate model should reproduce three main stages of keyhole evolution (its growth, excitation of oscillations, and collapse). The specifics of TC flow in the DP mode determine the nature of keyhole evolution under prolonged exposure to stationary radiation with a characteristic final (3rd) stage of flow-in and keyhole collapse under ongoing irradiation. This 3rd stage is of no interest for technological applications, but allows one to determine explicitly the main hydrodynamic mechanism in the DP mode, which makes it important for model validation.

It is instructive to compare the results of computer visualization with X-ray imaging data [43] (Fig. 9). Numerical calculations of the evolution of hydrodynamic parameters at the initial stage of melting (similar to the evaluation analysis in Section 4) are also important for testing the veracity of models. It is advisable to compare the calculated TC flow velocity with measurement data [50]. It should be noted that a physically justified discretization of the computational domain and time, which, apparently, will require significant (supercomputer) computing resources, is needed for correct reproduction of TC flow.

The reproduction of shear structure of TC flow at the keyhole growth stage (1st stage of evolution) is of particular importance for modeling of manufacturing processes. The velocity of such flow reaches its maximum on the free surface of the melt (formula (1)) and is equal to zero at the melting boundary. Thickness $h = \delta$ of shear TC flow (or viscous sublayer) is estimated using formula (2) and is specified by the condition of equality of the deformation rate of the free surface and the melting front velocity ($V_S = V_M$). While the melting boundary is characterized by melting point TM, the liquid–gas surface is heated, according to experiments [39], to TB. Thus, temperature gradient $(T_B - T_M)/h$ is present in the molten layer and

exerts a decisive influence on the threshold transition to the DP mode at $Aq_{th}(d) = \lambda(T_B - T_M)/h$. The correctness of formula (2) was confirmed conclusively by the correspondence of $AP_{th}(d) = Aq_{th}(d)(\pi d^2/4)$ calculations to 36 experimental points obtained in 25 studies for four metals (iron, titanium, copper, aluminum) (Figs. 12, 13). This confirms that, contrary to the common belief that a sharp increase in evaporation is critically important in this case, the transition to the DP mode is caused by a high TC flow velocity and rapid deformation of the free surface, which supports the shear structure of TC flow during the keyhole formation. The ingression of cold mass on a beam is what supports the shear structure of TC flow in experiments with beam scanning.

Having gained an insight into physical processes in the keyhole at the 2nd stage of its evolution and taken the influence of the beam scan rate into account, we formulated a physical interpretation of the pore formation trends observed in experiments in the DP mode. The results of pore formation analysis provide guidelines for computer modeling of this process and model validation. The criterion of a process window with zero pore generation by the keyhole is useful in practical applications as an opportunity for predictive determination of operational parameters of a defect-free process. This criterion may be used to digitalize the labor-intensive process of elaboration of a manufacturing process for high-duty products and to alter the parameters of a technological process in a flexible manner within the framework of an existing technology (or to transfer an existing technology from one facility to another). Practical implementation of these opportunities requires targeted research into the parameters of the technological window.

Building upon the understanding of the significance of capillary effects in manufacturing processes, we detailed the mechanism of influence of electrodynamic processes on the acceleration of TC flow of melt during DP of metals by high-power laser radiation. This mechanism establishes a connection between hydrodynamic processes and thermionic and electrocapillary effects. It provides a qualitative explanation of the experimentally observed patterns and may be used to improve process control and management.

In the present review, we endeavored to present a brief summary of certain aspects of the DP phenomenon that provide the key to understanding the technological processes governed by it. The physics of the phenomenon turns out to be quite diverse and is far from being fully investigated both theoretically and experimentally. Enough blank spots concealing the full potential of relevant technologies still remain. The nonlinear progress in understanding the nature of DP demonstrates that a closer and more targeted interaction and consolidation of the efforts of specialists from different fields of knowledge (physicists, process engineers, materials scientists, and computing engineers) are needed to reveal the technological potential of this phenomenon.

Acknowledgments

This study was carried out under the state assignment of the National Research Center „Kurchatov Institute."

Conflict of interest

The authors declare that they have no conflict of interest.

References

[1] V.Ya. Panchenko, V.S. Golubev, V.V. Vasil'tsov, M.G. Galushkin, A.N. Grezev, V.D. Dubrov, A.N. Evseev, A.N. Zharinov, Yu.N. Zavalov, A.Yu. Ivochkin, S.V. Kamaev, A.A. Karabutov, E.V. Kotsyuba, V.S. Maiorov, S.V. Maiorov, M.A. Markov, F.Kh. Mirzade, V.G. Niz'ev, A.N. Nikitin, M.M. Novikov, E.V. Savateeva, V.S. Solomatin, M.Yu. Sternin, V.P. Yakunin, A.G. Kaptil'nyi. *Lazernye tekhnologii obrabotki materialov: sovremennye problemy fundamental'nykh issledovanii i prikladnykh razrabotok*. Ed. by V.Ya. Panchenko (Fizmatlit, M., 2009) (in Russian).

[2] G.G. Gladush, I. Smurov. *Physics of Laser Materials Processing: Theory and Experiment* (Springer-Verlag, Berlin, 2011), 534 p.

[3] O.B. Kovalev, V.M. Fomin. *Fizicheskie osnovy lazernoi rezki tolstykh listovykh materialov* (Fizmatlit, M., 2013) (in Russian).

[4] J.L. Zou, Y. He, S.K. Wu, T. Huang, R.S. Xiao. Appl. Surf. Sci., **357**, 1522 (2015). https://doi.org/10.1016/j.apsusc.2015.09.198

[5] S.G. Gornyi, V.A. Lopota, V.D. Redozubov, I.G. Rudoi, A.M. Soroka, Yu.T. Sukhov. Zh. Tekh. Fiz., **57** (12), 2390 (1987) (in Russian).

[6] V.A. Batanov, V.B. Fedorov. ZhETF Pis. Red. **17** (7), 348 (1973).

[7] M.S. Baranov, B.A. Vershok, I.N. Geinrikhs. Teplofiz. Vys. Temp., **13** (3), 566 (1975) (in Russian).

[8] J.G. Andrews, D.R. Atthey. J. Phys. D: Appl. Phys., **9** (15), 2181 (1976).

[9] N.A. Ol'shanskii, A.M. Gutkin, G.I. Girimadzhi. Svar. Proizvod., **9**, 12 (1974) (in Russian).

[10] A.A. Bondarev, N.M. Voropai. Fiz. Khim. Obrab. Mater., **2**, 50 (1974) (in Russian).

[11] A.M. Verigin, A.A. Erokhin, V.N. Shavyrin, V.F. Reznichenko. Fiz. Khim. Obrab. Mater., **2**, 145 (1980) (in Russian).

[12] V.F. Reznichenko, A.M. Verigin. Svar. Proizvod., **6**, 25 (1986) (in Russian).

[13] S.I. Anisimov, Ya.A. Imas, G.S. Romanov, Yu.V. Khodyko. *Deistvie izlucheniya bol'shoi moshchnosti na metally* (Nauka, M., 1970) (in Russian).

[14] R. Fabbro, M. Hamadou, F. Coste. J. Laser Appl., **16** (1), (2004). https://doi.org/10.2351/1.1642633

[15] R.D. Seidgazov. *Laser Technologies in Welding and Material Processing. Proceedings of the Forth International Conference* (26–29 May, 2009, E.O. Paton Electric Welding Institute)

[16] R.D. Seidgazov. *IEEE 8th Int. Conf. on Advanced Optoelectronics and Lasers* (CAOL), (Sozopol, Bulgaria, 2009), 216 (2019). https://doi.org/10.1109/CAOL46282.2019.9019431

[17] J. Svenungsson, I. Choquet, A.F.H. Kaplan. Phys. Proced., **78**, 182 (2015). https://doi.org/10.1016/j.phpro.2015.11.042

[18] M. Courtois, M. Carin, Ph. Le Masson, S. Gaied, M. Balabane. J. Phys. D: Appl. Phys., **49**, 155503 (2016). https://doi.org/10.1088/0022-3727/49/15/155503
[19] R.D. Seidgazov. *Mikroskopicheskaya gidrodinamika pri plavlenii materialov lazernym izlucheniem* (Nauchno-Issled. Tsentr Tekhnol. Lazeram Akad. Nauk SSSR, 1987) (in Russian).
[20] R.D. Seidgazov, Yu.M. Senatorov, Sov. J. Quant. Electron., **18** (3), 396 (1988). https://doi.org/10.1070/QE1988v018n03ABEH011530
[21] R.D. Seidgazov. J. Phys. D: Appl. Phys., **42** (17), 175501 (2009). http://dx.doi.org/10.1088/0022-3727/42/17/175501
[22] R.D. Seidgazov. Mathematical Models and Computer Simulations, **3** (2), 234 (2011). http://dx.doi.org/10.1134/S2070048211020098
[23] R.D. Seidgazov, F.Kh. Mirzade, Technical Physics Letters, 2022, Vol. 48, No. 9. DOI: 10.21883/TPL.2022.09.55085.19283
[24] R.D. Seydgazov, F.Kh. Mirzade. Welding International, **35** (7–9), 359 (2021). http://dx.doi.org/10.1080/09507116.2021.1979829
[25] R.D. Seidgazov, F.Kh. Mirzade, Technical Physics Letters, 2023, Vol. 49, No. 6. DOI: 10.61011/TPL.2023.06.56384.19553
[26] R.D. Seidgazov, F.Kh. Mirzade. Chinese J. Mechan. Engineering: Additive Manufacturing Frontiers, **1** (3), (2022). http://dx.doi.org/10.1016/j.cjmeam.2022.100044
[27] R.D. Seidgazov, F.Kh. Mirzade. Tyazh. Mashinostr., (11–12), 46 (2024) (in Russian).
[28] H. Ki, P.S. Mohanty, J. Mazumder. Metallurgical Mater. Transactions A, 33A, 1817 (2002).
[29] H. Ki, P.S. Mohanty, J. Mazumder. Metallurgical Mater. Transactions A, 33A, 1831 (2002).
[30] J.Y. Lee, S.H. Ko, D.F. Farson, C.D. Yoo. J. Phys. D: Appl. Phys., **35**, 1570 (2002).
[31] N. Kouraytem, X. Li, R. Cunningham, C. Zhao, N. Parab, T. Sun, A.D. Rollett, D. Ashley. Spear, and Wenda Tan. Phys. Rev. Appl., **11**, 064054 (2019).
[32] S. Ly, G. Guss, A.M. Rubenchik, W.J. Keller, N. Shen, R.A. Negres, J. Bude. Scientific Reports, **9**, 8152 (2019). http://dx.doi.org/10.1038/s41598-019-44577-6
[33] R.D. Seidgazov, F.Kh. Mirzade. Math. Models Comput. Simul., **17** (1), 25 (2025). DOI: https://doi.org/10.20948/mm-2024-05-04 [R.D. Seidgazov, F.Kh. Mirzade. Mathematical Models and Computer Simulations, **17** (1), 25 (2025). http://dx.doi.org/10.1134/S2070048224700698]
[34] I.V. Krivtsun, V.Yu. Khaskin, V.N. Korzhik, E.V. Illyashenko, Ch. Dong, Z. Luo. Medical Sciences/„Colloquium-Journal", **18** (42), (2019). http://dx.doi.org/10.24411/2520-6990-2019-10596
[35] P.J. DePond, J.C. Fuller, S.A. Khairallah, J.R. Angus, G. Guss, M.J. Matthews, A.A. Martin. Communications Mater., **1** (92), (2020). http://dx.doi.org/10.1038/s43246-020-00094-y
[36] S.A.H. Fawzi, R.N. Arif. Tr. J. Phys., **23**, 959 (1999).
[37] R.D. Seidgazov, F.Kh. Mirzade, Technical Physics Letters, 2025, **49** (6) 61 DOI: http://dx.doi.org/10.61011/TPL.2025.06.61293.20184
[38] A. A. Vedenov, G.G. Gladush. *Fizicheskie protsessy pri lazernoi obrabotke materialov* (Energoatomizdat, M., 1985) (in Russian).
[39] K. Hirano, R. Fabbro, M. Muller. J. Phys. D: Appl. Phys., **44** (43), 435402 (2011). http://dx.doi.org/10.1088/0022-3727/44/43/435402
[40] J. Trapp, A.M. Rubenchik, G. Guss, M.J. Matthews. Appl. Mater. Today, **9**, 341 (2017).
[41] R. Fabbro. Appl. Sci., **10**, 1487 (2020). http://dx.doi.org/10.3390/app10041487
[42] C. Banas. Opt. Eng., **17** (3), 210 (1978).
[43] R. Cunningham, C. Zhao, N. Parab, C. Kantzos, J. Pauza, K. Fezzaa, T. Sun, A.D. Rollett. Science **363**, 849 (2019). http://dx.doi.org/10.1126/science.aav4687
[44] F.V Bunkin, M.I. Tribel'skiĭ. Phys. — Uspekhi, **23** (2), 105 (1980). https://doi.org/10.1070/PU1980v023n02ABEH004904
[45] R.D. Seidgazov, F.Kh. Mirzade. Tech. Phys. Lett., **14**, 12 (2022). http://dx.doi.org/10.21883/TPL.2022.14.52104.18838
[46] E.B. Levchenko, A.L. Chernyakov. Sov. Phys. JETP, **54** (1), 102 (1981).
[47] V.I. Ledenev, F.Kh. Mirzade. Quant. Electron., **23** (12), 1030 (1993). http://dx.doi.org/10.1070/QE1993v023n12ABEH003278
[48] F.Kh. Mirzade, V.Ya. Panchenko, L.A. Shelepin Phys. Usp., **39** (1), 1 (1996).
[49] S.V. Kayukov. Quant. Electron., **30** (11), 941 (2000). http://dx.doi.org/10.1070/QE2000v030n11ABEH001825
[50] I. Eriksson, J. Powell, A.F.H. Kaplan. Sci. Technol. Welding Joining, **16** (7), 636 (2011). http://dx.doi.org/10.1179/1362171811Y.0000000050
[51] T. DebRoy, S. Basu, K. Mundra. J. Appl. Phys., **70** (3), 1313 (1991).
[52] M. Eissen, D.M. Keicher. *Proc. of Society of Photo-Optical Instrumentation Engineers* (SPIE), **2993** (2), 2 (1997).
[53] F. Tenner, C. Brock F.-J. Gurtler, F. Klampf, M. Schmidt. Phys. Proced. 8th International Conference on Photonic Technologies LANE 2014, **56**, 1268 (2014).
[54] P.A.A. Khan, T. Debroy, S.A. David. Welding J., **67** (1), 1s (1988).
[55] Y. Kawahito, N. Matsumoto, Y. Abe, S. Katayama. Welding International, **27** (2), 129 (2013). http://dx.doi.org/10.1080/09507116.2011.606151
[56] W. Gatzweller, D. Maischner, F.J. Faber, C. Derichs, E. Beyer. Proc. SPIE, **1132**, 157 (1989).
[57] I. Myamoto, H. Maruo, Y. Arata. International Congress on Applications of Lasers and Electro-Optics (ICALEO) **44**, 68 (1984).
[58] A.N. Grezev. Weld. Int., **19**, 906 (2005).
[59] M. Ono, Y. Shimbo, M. Ohnura et al. NKK Tech. Rev., **77**, 48 (1997).
[60] S. Katayama. in *Handbook of Laser Welding Technologies* (ed. by S. Katayama) Elsevier Ltd, Oxford, UK, 2013), (http://dx.doi.org/10.1533/9780857098771.2.332)
[61] M. Tribel'skii. Sov. J. Quantum Electron., **8** (4), 462 (1978). [Sov. J. Quant. Electron., **8** (4), 462 (1978). https://doi.org/10.1070/QE1978v008n04ABEH010055]
[62] A. Russ, M. Leimser, F. Dausinger. Proc. of Society of Photo-Optical Instrumentation Engineers (SPIE), **5662**, (2004). http://dx.doi.org/10.1117/12.596352
[63] T. Graf, P. Berger, R. Weber, H. Hugel, A. Heider, P. Stritt. Laser Phys. Lett., **12**, 056002 (2015). http://dx.doi.org/10.1088/1612-2011/12/5/056002
[64] D.B. Hann, J. Iammi, J. Folkes. Proceedings of the 36th International MATADOR Conference, 275 (2010). http://dx.doi.org/10.1007/978-1-84996-432-6_63
[65] W.E. King, H.D. Barth, V.M. Castillo, G.F. Gallegos, J.W. Gibbs, D.E. Hahn, C. Kamath, A.M. Rubenchik. J. Mater. Processing Technol., **214**, 2915 (2014). http://dx.doi.org/10.1016/j.jmatprotec.2014.06.005

[66] N.P. Calta, A.A. Martin, J.A. Hammons, M.H. Nielsen, T.T. Roehling, K. Fezzaa, M.J. Matthews, J.R. Jeffries, T.M. Willey, J.R.I. Lee. Additive Manufacturing, **32**, 101084 (2020). http://dx.doi.org/10.1016/j.addma.2020.101084
[67] P.J. DePond, J.C. Fuller, S.A. Khairallah, J.R. Angus, G.Guss, M.J. Matthews, A.A. Martin. Commun. Mater., **1** (92), (2020). http://dx.doi.org/10.1038/s43246-020-00094-y
[68] H.N. Brahsch, D.C. Weckman, H.W. Kerr. Welding J., 6, 141s (1994).
[69] S. Zhao, L. Yang, Y. Huang, D. Zhao, S. Xu. Intern. J. Advanced Manufacturing Technol., **104**, 893 (2019). http://dx.doi.org/10.1007/s00170-019-03916-7
[70] E. Assuncao, S. Williams, D. Yapp. Optics Lasers Eng., **50**, 823 (2012). http://dx.doi.org/10.1016/j.optlaseng.2012.02.001
[71] S.D. Jadhav, L.R. Goossens, Y. Kinds, B. Van Hooreweder, K. Vanmeensel. Additive Manufacturing, **42**, 101990 (2021). http://dx.doi.org/10.1016/j.addma.2021.101990
[72] S. Engler, R. Ramsayer, R. Poprawe. Phys. Proced., **12**, 339 (2011). http://dx.doi.org/10.1016/j.phpro.2011.03.142
[73] M. Miyagi, X. Zhang. J. Laser Applications, **27** (4), 042005 (2015). http://dx.doi.org/10.2351/1.4927609
[74] E. Biro, D.C. Weckman, Y. Zhou. Metallurgical Mater. Transactions A, **33A**, 2019 (2002).
[75] P.D. Bono, I. Metsios, J. Blackburn, P. Hilton, 32-nd *International Congress on Applications of Lasers and Electro-Optics* (ICALEO-2013), http://dx.doi.org/10.2351/1.5062925
[76] V.N. Garashchuk, O.A. Velichko, V.B. Davydova. Avtom. Svarka, **5**, 31 (1971) (in Russian).
[77] A.A. Martin, N.P. Calta, S.A. Khairallah, J. Wang, P.J. Depond, A.Y. Fong, V. Thampy, G.M. Guss, A.M. Kiss, K.H. Stone, C.J. Tassone, J.N. Weker, M.F. Toney, T. van Buuren, M.J. Matthews. Nature Commun., **10**, 1987 (2019). http://dx.doi.org/0.1038/s41467-019-10009-2
[78] E. Soylemez.*Solid Freeform Fabrication 2018: Proc. of the 29th Annual Int. Solid Freeform Fabrication Symposium — An Additive Manufacturing Conference*, 1721 (2018).
[79] E. Akman, A. Demir, T. Canel, T. Sınmazcëelik. J. Mater. Processing Techn., **209**, 3705 (2009). http://dx.doi.org/10.1016/j.jmatprotec.2008.08.026
[80] Q. Guo, C. Zhao, M. Qu, L. Xiong, L.I. Escano, S.M.H. Hojjatzadeh, N.D. Parab, K. Fezzaa, W. Everhart, T. Sun, L. Chen. Additive Manufacturing, **28**, 600 (2019). http://dx.doi.org/10.1016/j.addma.2019.04.021
[81] H. Hügel, A. Ruß, J. Weberpals, F. Dausinger. Proc. of Society of Photo-Optical Instrumentation Engineers (SPIE), **5958**, 595807 (2005). http://dx.doi.org/10.1117/12.621616
[82] P. Stritt, R. Weber, T. Graf, S. Müller, C. Ebert. Phys. Procedia, **12**, 224 (2011). http://dx.doi.org/10.1016/j.phpro.2011.03.029
[83] D.C. Weckman, H.W. Kerr, J.T. Liu. Metallurgical Mater. Transactions B, **28B**, 687 (1997).
[84] P. De Bono, I. Metsios, J. Blackburn, P. Hilton, International Congress on Applications of Lasers & Electro-Optics (ICALEO-2013), http://dx.doi.org/10.2351/1.5062925
[85] Y.A. Mayi, M. Dal, P. Peyre, M. Bellet, C. Metton, C. Moriconi, R. Fabbro. J. Phys. D: Appl. Phys., **53**, 075306 (2020). http://dx.doi.org/10.1088/1361-6463/ab5900
[86] K.Q. Le, C. Tang, C.H. Wong. Intern. J. Thermal Sci., **145**, 105992 (2019). http://dx.doi.org/10.1016/j.ijthermalsci.2019.105992
[87] P. Ninpetch, P. Kowitwarangkul, S. Mahathanabodee, P. Chalermkarnnon, P. Rattanadecho. Case Studies Thermal Eng., **24**, 100860 (2021). http://dx.doi.org/10.1016/j.csite.2021.100860
[88] H. Gong, K. Rafi, H. Gu, T. Starr, B. Stucker. Additive Manufacturing, (2014), http://dx.doi.org/10.1016/j.addma.2014.08.002
[89] C. Taute, H. Müller, A. du Plessis, M. Tshibalanganda, M. Leary. J. Southern African Institute Mining Metallurgy, **121** (4), 143 (2021). http://dx.doi.org/10.17159/2411- 9717/1331/2021
[90] M. Tang, P.C. Pistorius, J.L. Beuth. Additive Manufacturing, **14**, 39 (2017). http://dx.doi.org/10.1016/j.addma.2016.12.001

Translated by D.Safin